

Molecular tuning of excitons and polarization anisotropy in hybrid bilayer crystals

Authors:

Tomojit Chowdhury^{1,2,10}, Aurélie Champagne^{3,4,10}, Fauzia Mujid¹, Patrick Knüppel⁵, Zehra Naqvi⁶, Ce Liang⁶, Ariana Ray⁷, Mengyu Gao¹, David A. Muller⁷, Nathan Guisinger⁸, Kin Fai Mak⁵, Jeffrey B. Neaton^{3,4,9}, & Jiwoong Park^{1,2,6*}

Affiliations:

¹Department of Chemistry, University of Chicago, Chicago, IL, USA

²James Franck Institute, University of Chicago, Chicago, IL, USA

³Department of Physics, University of California, Berkeley, CA, USA

⁴Materials Science Division, Lawrence Berkeley National Laboratory, Berkeley, CA, USA

⁵Department of Physics, Cornell University, Ithaca, NY, USA

⁶Pritzker School of Molecular Engineering, University of Chicago, Chicago, IL, USA

⁷Department of Applied and Engineering Physics, Cornell University, Ithaca, NY, USA

⁸Center for Nanoscale Materials, Argonne National Laboratory, Lemont, IL, USA

⁹Kavli Energy Nanoscience Institute, University of California, Berkeley, CA, USA

¹⁰These authors contributed equally to this work

*corresponding author: jwpark@uchicago.edu

Abstract:

Bilayer crystals, built from monolayers of two-dimensional (2D) crystals with different lattice orientations, generate interlayer potentials leading to unique excitonic properties¹⁻⁵. However, the ability to tune the interlayer potential is limited by the fixed covalent 2D lattice geometries. Synthetically substituting one of the layers with an atomically thin molecular crystal could substantially expand the design space for tuning the excitonic response⁶, enabled by explicit control of chemical and electronic structures of the molecular building blocks⁷⁻⁹. Here we report the large-scale synthesis of four-atom-thick hybrid bilayer crystals (HBCs), comprising perylene-based molecular and transition metal dichalcogenide (TMD) monolayer single crystals, which show precise tuning of the HBC lattices at the molecular level. We observe near-unity anisotropic photoluminescence, which is directly tuned by specific molecular geometry and HBC composition. Our ab initio GW and Bethe-Salpeter equation calculations show that the anisotropic emission originates from delocalized and anisotropic hybrid excitons. These excitons inherit characteristics from states associated with both the TMD and molecular layers, resulting from a hybridized bilayer band structure of the HBC. By introducing HBCs as a scalable solid-state platform, our work paves the way for tunable interlayer energy landscapes achievable through direct synthesis, opening up new frontiers in molecule-based quantum materials.

Conventional bilayer crystals are built by stacking two mechanically exfoliated covalent 2D crystals (e.g. graphene, TMDs), each with different lattices or orientations, to generate an interlayer potential. The tunable nanoscale spacing of this interlayer or moiré potential results in emergent phenomena including exciton insulators², Mott insulators¹⁰, superconductivity¹¹, and Wigner order¹²⁻¹⁴. However, in these bilayer crystals, the interlayer potential is primarily governed by the relative orientation of fixed structures, predominantly honeycomb lattices, of the constituent covalent 2D crystals, which limits the tunability and symmetry of the resulting materials. Replacing one of the layers with a molecular crystal through direct synthesis, thereby forming a hybrid bilayer crystal (HBC), provides powerful and additional tuning knobs to address these limitations by leveraging the vast modularity of molecular building blocks in both structures and properties⁷, which cannot be achieved in conventional bilayers. A free-standing, monolayer molecular crystal generates a periodic array of localized one-electron states with the lattice spacing and symmetry controlled by the geometry of the single molecular units and the non-covalent intermolecular interactions¹⁵⁻¹⁷. Its localized electron wavefunctions, derived from highest occupied and lowest unoccupied molecular orbitals (HOMOs and LUMOs) of the individual molecular monomers, can lead to electronic bands for the 2D monolayers with negligible dispersion and localized excitons¹⁸. Within an HBC, however, these one-electron states may interact with the delocalized states of the semiconducting covalent 2D crystal, potentially leading to intra- and interlayer delocalization¹⁹⁻²¹. This interaction can result in a hybridized bilayer band structure with greater dispersion, allowing the excitons to be delocalized significantly in real space while also retaining molecule-like properties, including strong optical anisotropy (**Fig. 1a**).

This makes HBCs a tunable platform for exploring novel excitonic phenomena, but harnessing their full potential entails a systematic approach that encompasses three major elements: (1) large-scale synthesis of HBCs with superior single-crystallinity; (2) molecule-level tuning of HBC lattice and exciton anisotropy; and (3) state-of-the-art *ab initio* theory to elucidate molecularly tunable bilayer band structures and the nature of excitons (localized vs. delocalized) in HBCs. While previous studies have highlighted the promise of molecule-based 2D solids and their heterostructures^{15,16,20-26}, there currently exists no report of a systematic demonstration showing the molecular tuning of lattices and exciton anisotropy, achieved via direct synthesis, on an atomically thin and scalable HBC platform.

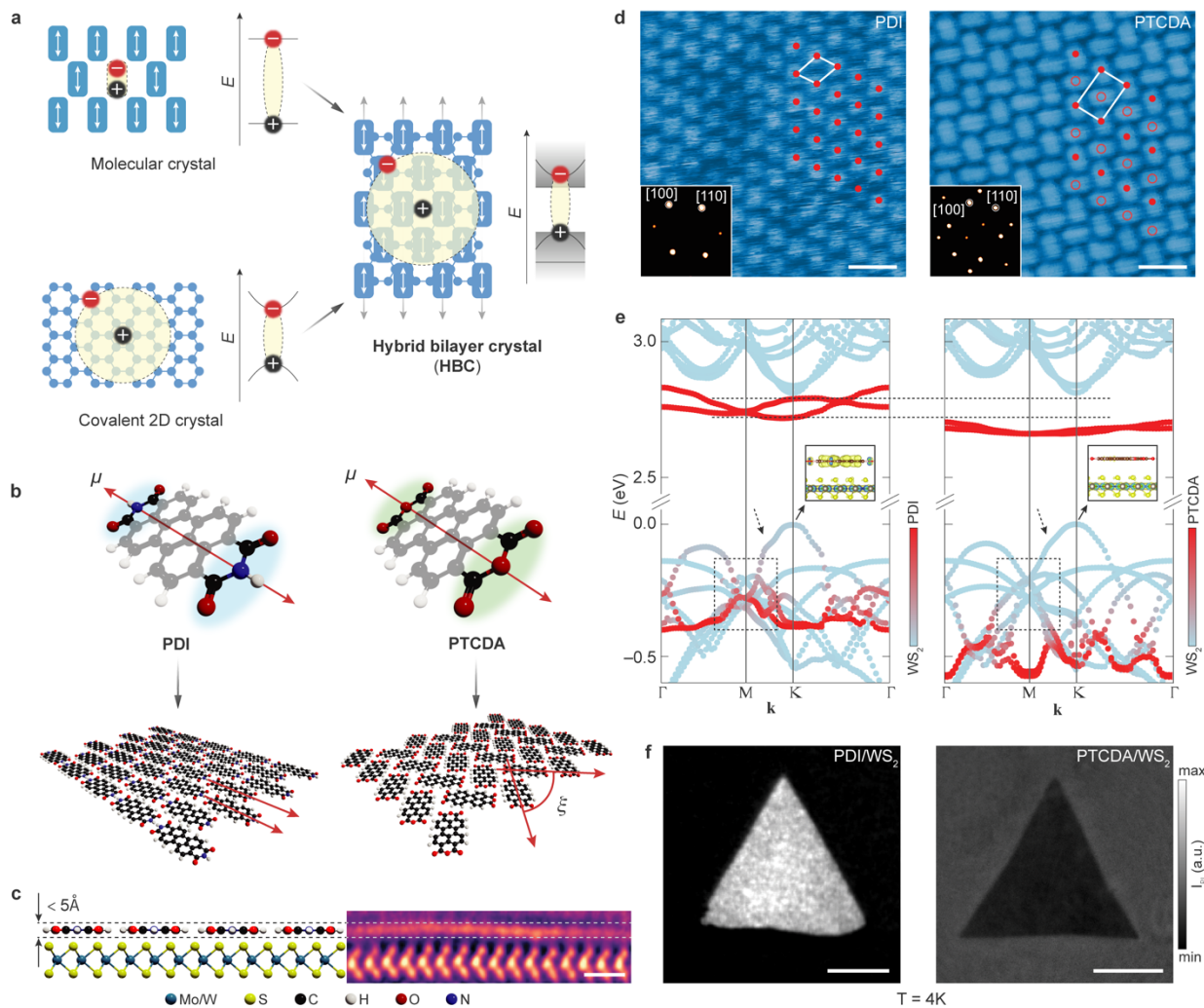


Figure 1. Molecular tuning of HBC lattices and band structures. (a) Schematic illustrating the generation of HBCs from molecular and covalent 2D crystals with their associated exciton energy diagrams. White (gray) double-sided arrows denote single-molecular (crystal) polarization directions. (b) Ball-and-stick models of PDI and PTCDA molecules showing single-molecule dipole moments (μ ; red double-sided arrows) (top). Energy-optimized structures of freestanding monolayer molecular crystals (bottom). The misorientation angle between the dipolar axes is denoted by ζ . (c) Ball-and-stick model of a four-atom-thick HBC (left) shown along with a representative cross-sectional ac-STEM image of a PDI/MoS₂ domain (right). Dashed grey line highlights one-atom-thick molecular monolayer. Scale bar: 1 nm. (d) Room-temperature STM images of PDI and PTCDA grown on monolayer MoS₂. Solid and open red dots denote molecular lattice points. Molecular unit cells are highlighted with white boxes. *Insets*: FFT of the molecular lattices. Scale bar: 2 nm. (e) GW band structures of PDI/WS₂ (left) and PTCDA/WS₂ (right) highlighting the features of orbital hybridization by dashed arrows, lines, and boxes. Red (light-blue) color denotes contributions from molecular (WS₂) electronic states. *Insets*: Computed real-space VBM-HOMO wavefunctions at the K point. (f) Wide field polarized PL images of PDI/WS₂ (left) and PTCDA/WS₂ (right) acquired at a photon energy of ~ 2.15 eV at T = 4K (I_{PL} : PL intensity). Scale bar: 20 μ m.

Lattice and band structure of HBC single crystals

Figure 1 introduces our single crystalline HBC systems whose lattice structures are tuned synthetically at the molecular level. **Fig. 1b** shows molecular crystals of two perylene derivatives (more shown in **Fig. 4**), which share a two-fold symmetric aromatic core but differ only in the atomic substitution at peri positions: $-O-$ (PTCDA; right) vs $N-H$ (PDI; left). These are optically anisotropic building blocks with similar absorption and emission spectra, with the primary transition dipole moment (μ) oriented along the long axis²⁷. The 2D molecular lattice structures, including the misorientation angle (ζ) between neighboring molecules, can be controlled by the atomic substitutions that directly affect intermolecular interactions (**Fig. 1b**). Our HBCs are synthesized in two steps; first, we grow monolayer TMD single crystals (MoS_2 , WS_2) via metal organic chemical vapor deposition (MOCVD)²⁸ and then perform self-limited physical vapor deposition (PVD) that is carefully optimized to form large single-domain molecular crystals on TMD surfaces (see Methods).

The single crystal structures and the molecular level tuning in our HBCs are confirmed by atomic-resolution imaging. Atomic force microscopy (AFM) corroborates the single-atom-thickness of less than 5 Å and high spatial uniformity of the molecular crystal atop monolayer TMD (Supplementary Fig. 1). The cross-sectional aberration corrected scanning transmission electron microscopy (ac-STEM) image (**Fig. 1c** and Methods) confirms our HBC's four-atom-thickness with the average center-to-center distance of ~ 5 Å. **Figure 1d** shows scanning tunneling microscopy (STM) images of the distinctive molecular lattices of PDI (left) and PTCDA (right) crystals on monolayer MoS_2 (Methods). Both PDI and PTCDA crystals consist of nearly hexagonal 2D lattices (insets; **Fig. 1d**). They have similar structures and intermolecular spacing (Supplementary Fig. 2 and Supplementary Table 1), as shown by the overlaying arrays of red dots, with one significant difference. In PDI (**Fig. 1d**; left), the molecules are closely aligned with ζ near 0° (Supplementary Fig. 3), forming a brick-wall pattern with primitive cells (white box) containing a single-molecule basis (solid dots)²⁹. This is different from the previous observations in PDI on bulk MoS_2 ^{21,30}. In contrast, PTCDA (**Fig. 1d**; right) has a two-molecule basis (solid and open dots), with half of the molecules misoriented by about 76° to form a herringbone pattern consistent with previous studies^{22,23}. Additional optical measurements show a distinct splitting in the polarized reflection spectra (Supplementary Fig. 3), indicative of Davydov doublets²⁶, only in PTCDA but entirely absent in PDI. This is consistent with the molecular unit cell with a basis of 2 in PTCDA

and 1 in PDI. The PDI monolayer has the smallest primitive cell ($\sim 1 \text{ nm}^2$), which is half that of PTCDA. Another substitution from N-H in PDI to N-CH₃ results in an even larger unit cell ($\sim 3 \text{ nm}^2$) and a different ζ , around 27° (Supplementary Fig. 4).

The molecular tuning of HBC lattices leads to notable differences in electronic band structures. **Figure 1e** compares the band structures of PDI/WS₂ (left) and PTCDA/WS₂ (right) from our ab initio GW calculations (Methods; Supplementary Fig. 5)^{31–33}, color-coded by the relative orbital contributions: red (blue) corresponding to molecular (TMD) monolayers and pink to hybridized states. The band structure of PDI/WS₂ cannot be predicted based on a simple superposition of those of its constituents, exhibiting features that differ significantly from the nearly flat bands of an isolated PDI monolayer and the characteristic dispersive bands of WS₂ monolayers (Supplementary Fig. 6). First, the energies of bands with dominant HOMO and LUMO character (red color) in the HBC undergo a significant renormalization relative to their counterparts in the molecular monolayer due to nonlocal dielectric screening from the WS₂ layer. Second, the HBC bands with dominant LUMO character show noticeable dispersion and lifted degeneracy (dashes). Third, the HOMO bands with significant WS₂ character (pink; boxes) and the WS₂ valence bands with additional shoulders (arrows) indicate strong orbital hybridization. In contrast, the PTCDA/WS₂ shows much flatter LUMO-derived bands and negligible change to the WS₂ valence bands, as also shown in the valence band maxima (VBM)-HOMO wavefunctions at K point of the Brillouin zone (insets; **Fig. 1e** and Supplementary Fig. 7). The overall band alignments predicted in **Fig. 1e** are consistent with our electrochemical transport measurements (Supplementary Fig. 8). The unique electronic structure of these molecularly tuned HBCs has notable consequences for their photo-physics, resulting in surprising photoluminescence (PL). **Figure 1f** compares the low-temperature ($T = 4\text{K}$) co-linearly polarized PL images of PDI/WS₂ (bright PL) and PTCDA/WS₂ (dark) single crystals, measured near the molecular emission maxima ($\sim 2.15 \text{ eV}$; see Methods and Supplementary Fig. 9 for experimental details). This bright PL from PDI/WS₂ above the WS₂ excitonic gap ($\sim 2.0 \text{ eV}$)²⁸ is counterintuitive, as the PL from higher-energy excitons in PDI crystals is expected to be quenched due to the close spatial proximity ($\sim 5 \text{ \AA}$) of lower-energy WS₂ exciton states^{19,34}. Indeed, no such signal is observed from PTCDA/WS₂ (Extended Data Fig. 1b, d), consistent with the expected PL quenching, but a similarly bright PL is observed from PDI/MoS₂ (Extended Data Fig. 2). This anomalous PL emission and corresponding excitonic behavior in PDI-based HBCs are further discussed below (**Fig. 2** and **3**).

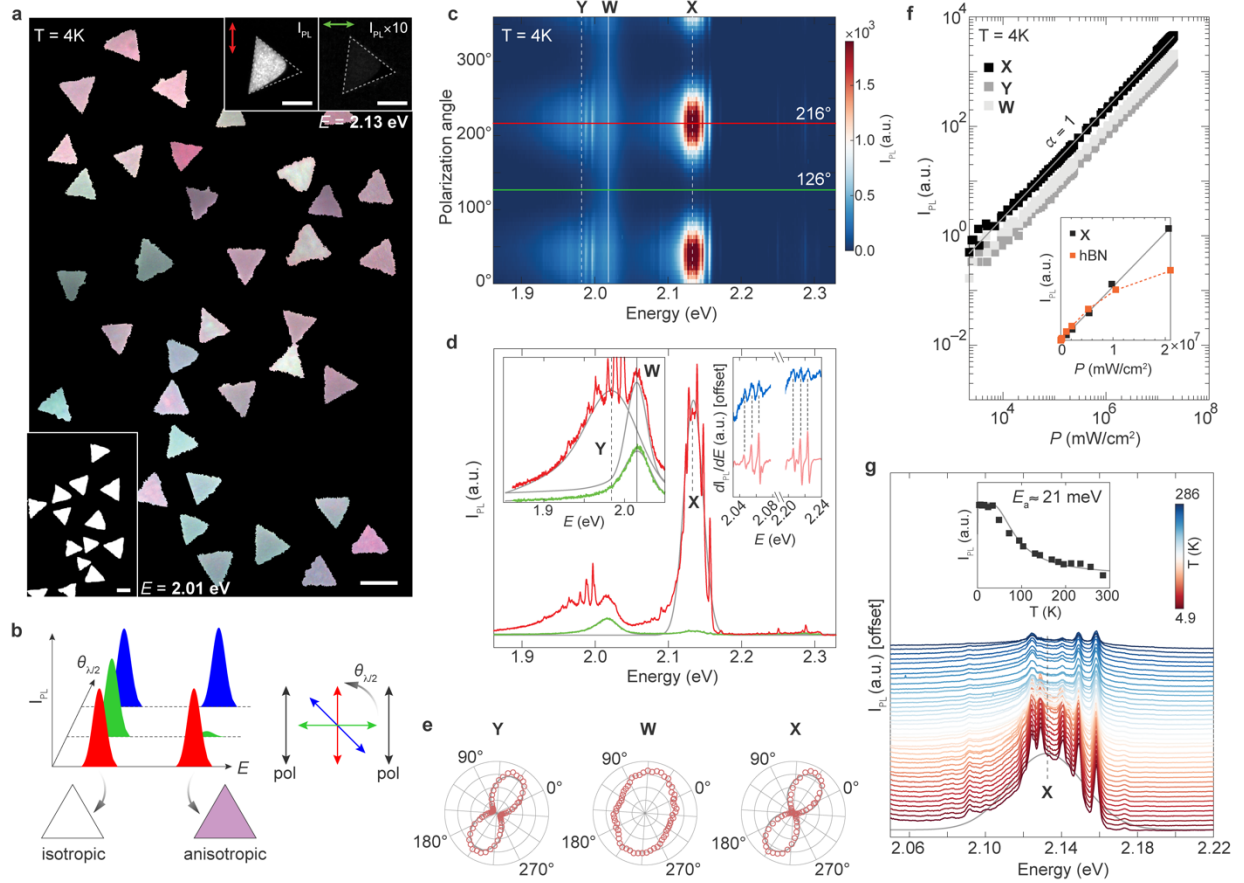


Figure 2. Above-gap polarized PL in PDI/WS₂. (a) Colinearly polarized PL RGB image of single-crystal islands at $E = 2.13$ eV. Scale bar: 20 μm . *Insets*: Co-polarized PL images of a partially grown PDI on WS₂ monolayer at two orthogonal polarization directions indicated as double-sided red and green arrows (top right); PL RGB image of single-crystal islands at $E = 2.01$ eV (bottom left). Scale bar: 10 μm . (b) Plot illustrating isotropic and anisotropic I_{PL} as a function of $\theta_{\lambda/2}$ and E . The RGB imaging scheme is shown on the right ($\theta_{\lambda/2}$: angle of the half-wave plate). (c) Polarization angle-dependent confocal PL map collected from a single crystal island highlighting three peaks—X, Y (dotted white lines), and W (solid white line). (d) PL spectra generated from the linecuts in (c) at two orthogonal polarization angles. Raw data shown with Gaussian overlays (grey lines). *Insets*: Zoomed-in spectral range below the WS₂ gap (left); dI_{PL}/dE vs. energy plot highlighting main Raman features with dashed black lines in the unshifted (blue; $E_{\text{ex}} = 2.38$ eV) and shifted (faded-red; $E_{\text{ex}} = 2.32$ eV) spectra (right). (e) Polar scatter plots for peaks X, Y, and W generated from (c), with overlaid cosine-squared fits for X and Y. (f) Logarithmic plot of power-density (P) dependent I_{PL} for X, Y, and W, with a solid gray line indicating a linear fit with unity exponent ($\alpha = 1$). *Inset*: Comparison of P -dependent I_{PL} for X and PDI/hBN. The solid gray line shows a linear fit (slope = 1), and the orange dotted line serves as a visual guide. (g) Temperature-dependent PL spectra highlighting peak X (dotted black line). *Inset*: Plot of I_{PL} vs. temperature for X with a single-exponential fit.

Strong PL anisotropy in single crystal PDI/WS₂

The bright above-gap PL signal ($E = 2.13$ eV) exhibits a full linear polarization as shown in **Fig. 2a** (top inset). **Figure 2a** (main panel) shows a false-colored wide-field PL image of PDI/WS₂ single crystals, revealing a distinct and uniform PL anisotropy direction for each single-crystal domain (see also Supplementary Video 1). The image is constructed by recording colinearly polarized PL intensity (I_{PL}) images at three polarization orientations ($\theta = 0^\circ, 45^\circ$ and 90°) and then color-coding and combining them as red (R), green (G), blue (B) channels (schematic in **Fig. 2b**). In contrast to the colorful triangles seen at 2.13 eV, the same imaging scheme conducted with the near-gap PL at 2.01 eV produces white triangles (bottom inset; **Fig. 2a**), suggesting significantly more isotropic PL.

The θ -dependent PL spectral map (**Fig. 2c**) and line spectra (**Fig. 2d**) acquired from a single-crystal PDI/WS₂ highlight three major PL peaks. Among these, **X** ($E_{\text{X}} = 2.13$ eV), which corresponds to the PL signal in **Fig. 2a**, is the brightest with its energy close to the molecular (PDI) absorption energy (Extended Data Fig. 3a). It is completely polarized exhibiting PL polarization anisotropy (φ) close to unity ($\varphi = 0.97$; **Fig. 2e**, right; see Supplementary Information for details). In contrast, **W** ($E_{\text{W}} = 2.01$ eV) has a significantly lower PL intensity and weaker anisotropy (**Fig. 2e**, middle; $\varphi = 0.24$), consistent energetically with the neutral excitons in monolayer WS₂^{28,35}. Importantly, we observe another anisotropic peak **Y** ($E_{\text{Y}} = 1.98$ eV) just below **W**, with its polarization dependence mirroring that of **X** (**Fig. 2e**, left; $\varphi = 0.83$). In addition, two groups of sharp (bandwidths ~ 2 – 3 meV) peaks, consistent with Raman active aromatic C=C vibrational modes^{36,37}, appear around **X** and **Y**, as confirmed by comparing the spectra measured at two excitation energies (**Fig. 2d**, right-inset and Supplementary Fig. 10). These observations suggest that **X** and **Y** are associated with excitons in anisotropic PDI molecules.

However, the high PL intensity of **X** and the presence of **Y** indicate unique excitonic properties associated with the HBC, distinguishing them from single molecules and molecule-based solids commonly explained in terms of localized (Frenkel) excitons. First, the PL bandwidths of **X** (34 meV) and **Y** (55 meV) are significantly broader—ranging from four to ten times wider—than those of structurally similar pristine molecular crystals^{38,39}, but are comparable to that of **W** (50 meV). Second, the excitation power-dependent PL response of **X** and **Y** closely resembles that of **W**, with all three following a linear relation (**Fig. 2f**). This suggests that the power-dependent behavior of **X** and **Y** excitons are similar to **W**. Together, these points rule out non-linear phenomena observed

in molecular aggregates. This is further supported by the differing power-dependent PL responses of PDI/hBN—a proxy for freestanding PDI—and **X**, where the former saturates and deviates from linearity, suggesting localized (PDI/hBN) and delocalized (**X**) excitonic behavior (**Fig. 2f**; inset)⁴⁰. Third, the exciton activation energy for **X** (~21 meV) in PDI/WS₂, as estimated from temperature-dependent PL spectra (**Fig. 2g** and Extended Data Fig. 1a, c), is almost an order of magnitude smaller than in pristine perylene derivatives⁴¹, indicating that excitons associated with **X** are more easily de-excited than the Frenkel excitons in molecules. Fourth, the peak **Y** is unlikely to result from excimer formation, which typically occurs in thicker organic films^{42,43}, as our HBCs consist of one-atom-thick molecular monolayers (**Fig. 1c**), showing no prominent PL peaks below 1.9 eV (Supplementary Fig. 11). Instead, the intensity, energy, and anisotropy of **X** and **Y** are tuned by the specific monolayer molecular lattice and TMD in the HBC, suggesting correlated contributions from excitons in molecules and the TMD monolayer. First, they are present only in PDI-based HBCs, disappearing altogether in PTCDA/WS₂ (**Fig. 1f**, right and Extended Data Fig. 1). Second, the intensity and anisotropy of **X** ($E_X = 2.12$ eV) in PDI/MoS₂ ($\varphi \sim 0.8$) become weaker than in PDI/WS₂, while **Y** ($E_Y = 1.96$ eV) is found above, not below, the isotropic MoS₂ PL peak (1.91 eV; Extended Data Fig. 2).

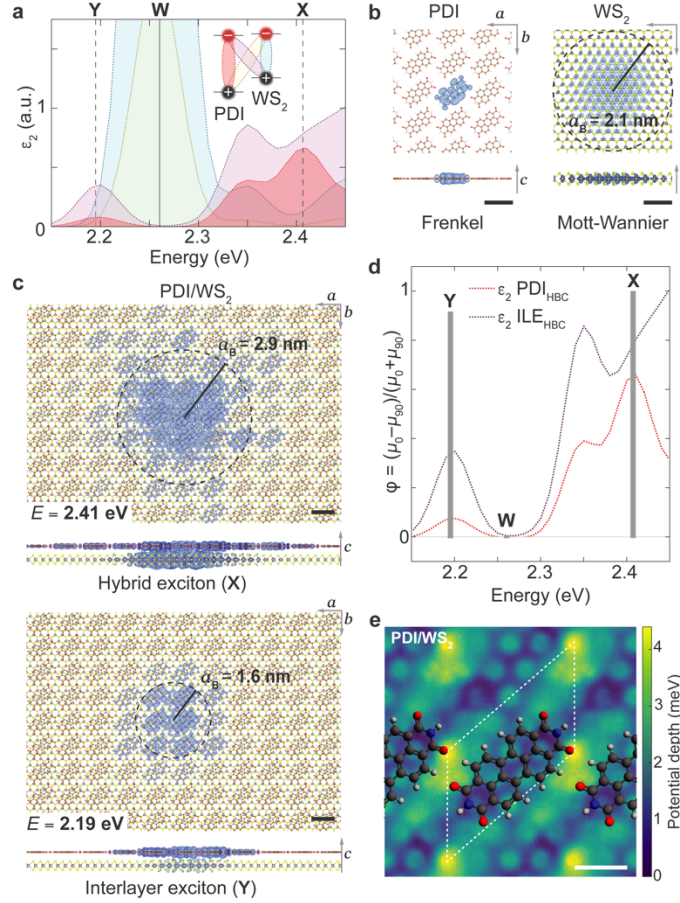


Figure 3. Delocalized excitons and polarization anisotropy in PDI/WS₂. (a) Computed imaginary components of the dielectric function (ϵ_2) of the HBC plotted against energy, showing contributions from excitons predominantly associated with PDI (red), WS₂ (light-blue), and interlayer excitations (ILE) at low (pink) and high (yellow) energies. Peaks X and Y are marked with dashed lines and W with solid line. *Inset*: Schematic of the band alignment showing the four distinct excitonic species. (b) GW-BSE isosurface maps of the exciton wavefunctions (selected to include 98% of the electron density), showing the electron probability density (blue) given the most probable hole positions, projected on the a - b plane and along the c -axis for a Frenkel exciton (left) and a Mott-Wannier exciton (right) in freestanding PDI and WS₂ monolayers (a_B = Bohr radius). Scale bar: 1 nm. (c) Similar projections onto a $20 \times 20 \times 1$ supercell consisting of PDI and WS₂ monolayers together, highlighting excitons X (top) and Y (bottom) each with their respective energies and a_B . Scale bar: 1 nm. (d) Anisotropy in oscillator strength (ϕ) plotted against energy, highlighting peaks X, Y, and W, with overlaid dotted lines showing the PDI (red) and low-energy ILE (pink) contributions to the total absorption spectrum of the HBC. (e) Computed interlayer potential depth induced by the undoped PDI monolayer on the WS₂ surface. Dashed white lines highlight the periodicity of the potential energy landscape. Scale bar: 1 nm.

Ab initio calculations of excitons and polarization anisotropy in HBC

We perform ab initio GW and Bethe-Salpeter equation (BSE) calculations to gain insights into the nature of excitons in the HBC and the origins of the polarization anisotropy (see Methods and Supplementary Information for details). **Figure 3a** plots four components of the imaginary part of the dielectric function, ϵ_2 , directly related to the linear absorption spectrum for PDI/WS₂, each representing transitions associated with PDI (red), WS₂ (cyan), and interlayer excitations (ILE) at low (pink) and high (yellow) energy states (inset; **Fig. 3a** and Supplementary Fig. 12)⁴⁴. We identify three main features from our calculations at 2.19 eV, 2.27 eV, and 2.41 eV with their energy ordering consistent with the measured PL peaks: **X** appearing above **W**, and **Y** slightly below **W** (**Fig. 2c**). We generate real-space exciton maps by plotting the electron-hole correlation function for different excited states (Methods)^{45,46}. **Figure 3b** shows the real-space electron-hole correlation function of the primary excitonic states for freestanding monolayer crystals with typical Frenkel-like (left) and Mott-Wannier-like (right) excitons for PDI and WS₂ monolayers, respectively.

Figure 3c shows similar GW-BSE mapping for two excitonic states at 2.41 eV (top) and 2.19 eV (bottom) in PDI/WS₂, which we assign as those corresponding to **X** and **Y**, respectively. They reveal in-plane delocalization over the HBC with the estimated exciton Bohr radii (a_B) of 2.9 nm for **X** and 1.6 nm for **Y** (Supplementary Table 2), with both comparable to that of an intralayer, Mott-Wannier-like exciton ($a_B = 2.1$ nm) confined within the WS₂ monolayer (Supplementary Fig. 13). The vertical distributions of the excitonic wavefunctions, however, differ markedly for **X** and **Y**: For **Y**, the electron density is confined primarily within the PDI layer, separated from the fixed hole in the WS₂ layer, suggesting an interlayer or charge-transfer character^{47,48} of the exciton (pink in **Fig. 3a**). For **X**, however, the electron density shows a significant vertical delocalization across both the WS₂ and PDI layers (see also Supplementary Fig. 14). Combined with our analysis of the PL data, this would suggest that **X** is associated with a hybrid exciton, involving both intra- and interlayer transitions (red and pink; **Fig. 3a**). The presence of hybrid exciton in PDI/WS₂ is attributed to the strong hybridization and orbital overlap between the HOMO and VBM, as shown in **Fig. 1e** (see also Supplementary Fig. 7). In contrast, the much weaker HOMO-VBM overlap in PTCDA/WS₂ explains the absence of a hybrid exciton, which is consistent with our PL experimental data.

The linear polarization anisotropy associated with each exciton, computed from the oscillator strengths for parallel and perpendicular polarizations (Supplementary Fig. 15), is plotted in **Fig. 3d** (grey bars). We note that the excitons above 2.3 eV are of hybrid character, with varying contributions from the PDI layer, resulting in more or less pronounced anisotropic response. Exciton **X**, which has the highest contribution from PDI (red, **Fig. 3a**), displays near-unity polarization anisotropy ($\varphi \sim 1$). In contrast, **W** shows negligible polarization dependence ($\varphi \sim 0$), while exciton **Y** showing significant anisotropy ($\varphi > 0.9$). This shows that the magnitude of polarization anisotropy is sensitive to the relative contribution of the molecular wavefunction to the hybrid (**X**) or interlayer (**Y**) excitons and originates from hybridization between the molecular and TMD wavefunctions. A recent study also reported below-gap excitons in PTCDA/WSe₂ interface with hybrid nature⁴⁹, without considering the 2D structure of the molecular crystals or the anisotropy it introduces. Our results, corroborated by this study, convey a common message: molecular crystals offer unique opportunities for tuning excitons in condensed matter systems (e.g., TMDs) in previously unexplored ways.

Beyond hybrid excitons, another important feature of HBCs is the interlayer potential energy landscape induced by the molecular monolayer. Our calculations show that even an undoped PDI monolayer induces a potential depth of ~ 4.5 meV at the WS₂ surface (**Fig. 3e**). Although shallower than those reported in all-inorganic moiré bilayers^{3,50}, this depth indeed creates a distinct charge localization pattern that aligns with HBC's periodic structure (white dashed line in **Fig. 3e**). This pattern correlates with the exciton wavefunction, with the electronic isosurface localizing in regions of lower potential (Supplementary Fig. 16). Together, the hybrid excitonic behavior and interlayer potential pose HBCs as a promising quantum materials platform for achieving tunable excitonic and moiré effects.

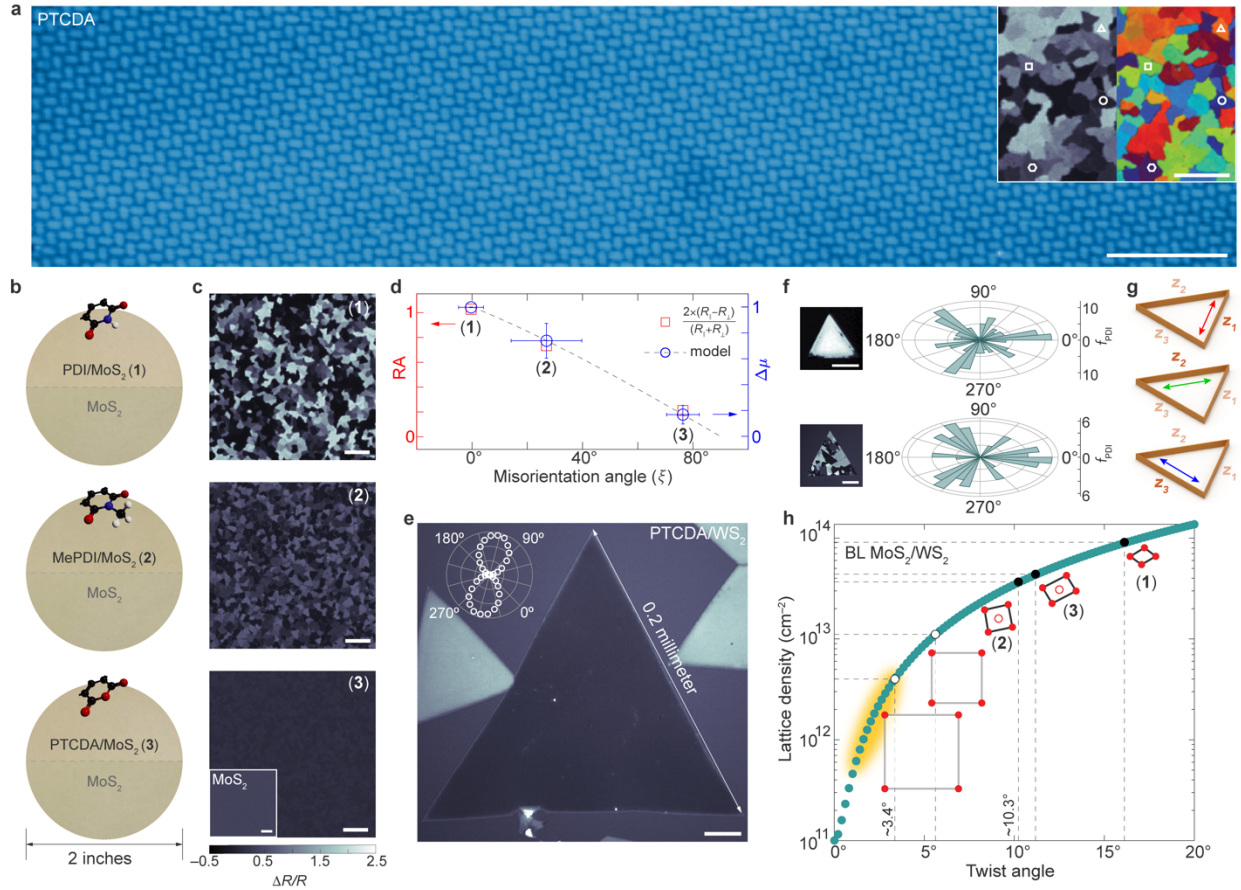


Figure 4. Large-scale HBCs with tunable properties. (a) STM image of an as-grown single-crystal PTCDA domain on monolayer MoS₂. Scale bar: 10 nm. *Inset*: $\Delta R/R$ (left) and false-colored RGB (right) images of polycrystalline PTCDA/MoS₂, showing microscopic domain structures and orientations. Geometric markers highlight distinct single-crystal domains. Scale bar: 20 μm . (b) Real-color photographs of as-grown PDI/MoS₂ (1), MePDI/MoS₂ (2) and PTCDA/MoS₂ (3) (upper-half) and monolayer MoS₂ (lower-half) on 2" fused silica wafers. Ball-and-stick models of corresponding perisubstitutions are shown side-by-side. (c) $\Delta R/R$ images of (1), (2), and (3) ($E \sim 2.2$ eV). *Inset*: $\Delta R/R$ image of MoS₂ ($E = 1.89$ eV). Scale bars: 20 μm . (d) Plot of measured reflection anisotropy (RA) and calculated $\Delta\mu$ as a function of ζ for (1), (2), and (3). (e) $\Delta R/R$ image of single crystal PTCDA/WS₂ domains ($E = 2.19$ eV). *Inset*: Characteristic polar plot from the domain. Scale bar: 20 μm . (f) θ -dependent polar histograms from reflection measurements of single-crystal (top) and polycrystalline (bottom) PDI domains on single-crystal WS₂, with representative reflectance images. Scale bars: 20 μm . (g) Schematic illustrating the relative orientation of triangular single-crystal TMD domains with three equivalent zigzag edges (z_1, z_2, z_3) and the molecular dipole vectors shown as double-sided arrows in red, green, and blue. (h) Lattice density vs. twist angle phase-space generated numerically for bilayer (BL) MoS₂/WS₂. Dashed lines indicate equivalent lattice densities and projected twist angles for (1), (2), and (3). Solid circles: our data; open circles: from literature,^{17,51} respectively. The critical low-density regime is highlighted by shaded region.

Large-scale synthesis and polarization tuning of HBC library

This striking excitonic behavior underscores the importance and potential use of large-scale synthesis of different HBCs with tunable properties, as shown in **Fig. 4**. First, the macroscopic single-crystalline order of our HBCs is confirmed by STM and cross-polarized reflection contrast ($\Delta R/R$) imaging at room-temperature. The STM image in **Fig. 4a** confirms the crystalline lattice of PTCDA on MoS₂, extending over 100 nanometers, free from imperfections, such as vacancies and mis-fit dislocations. Additionally, the continuous polycrystalline HBC domains are imaged through the angle dependence and spatial distribution of $\Delta R/R$ (inset, **Fig. 4a**; Supplementary Fig. 17), highlighting the spatial homogeneity of the molecular domains.

Wafer-scale continuous films of various HBCs are grown with controlled polycrystalline domain structures. **Figure 4b** shows unpolarized color photographs of three representative HBCs—PDI (**1**), MePDI (**2**), and PTCDA (**3**) monolayers on monolayer MoS₂—grown on 2” fused silica wafers (top-halves), with bare MoS₂ monolayers (bottom-halves) shown for comparison. All display inch-scale homogeneity with nearly identical color and contrast, reflecting the optical spectra of the common perylene core for **1–3** (Extended Data Fig. 3a). $\Delta R/R$ images (at ~ 2.2 eV) of three HBCs on transparent fused silica substrates show that the contrast between the maximum and the minimum within each image is highest in **1** and lowest in **3** with **2** staying between the two (**Fig. 4c**). We model the dipolar anisotropy ($\Delta\mu$) for **1–3** using a trigonometric relation and observe that the measured reflection anisotropy (RA) aligns with our model (**Fig. 4d** and Supplementary Fig. 18), demonstrating ζ as a synthetically tunable parameter for HBC polarization response. Altogether, we synthesize seven different HBCs (Supplementary Fig. 19, 20) and produce high-quality molecular lattices on other substrates, including graphene (Supplementary Fig. 21) and hexagonal boron nitride (Supplementary Fig. 22), showcasing the versatility of our synthesis method.

Figure 4e presents a $\Delta R/R$ image of PTCDA/WS₂ ($E \sim 2.2$ eV) synthesized with triangular WS₂ single crystals of size as large as 0.2 millimeter. The contrast varies significantly at the molecular absorption energy (Supplementary Video 2), following the characteristic polar plot (inset; **Fig. 4e**), but remains uniform at the TMD exciton energy (Supplementary Video 3). This behavior, consistent with our PL imaging (**Fig. 2a**), is observed across individual HBC domains, confirming the exceptional single crystallinity of the triangular HBC domains. $\Delta R/R$ imaging of poly- and single-crystalline PDI domains (inset, **Fig. 4a**; **4c**, **4e**) confirms that the size of the molecular

crystal domains closely resembles that of the underlying TMD, indicating that larger (smaller) HBC domains can be synthesized by using large (small) TMD domains.

Additional angle-dependent analysis of reflectance signals from both single-crystalline (**Fig. 4f**, top) and polycrystalline (**Fig. 4f**, bottom) PDI domains on single-crystal WS₂ shows an epitaxial relationship. The polar histograms display six peaks, each with two peaks within a 120° range (see also Supplementary Fig. 23). Based on the rotational symmetry of PDI (two-fold) and WS₂ (three-fold), this alignment indicates that the long-axis of PDI is aligned along one of the high symmetry axes of WS₂. With electron diffraction data confirming a zigzag edge termination of the WS₂ crystal, our data suggest that PDI is aligned along one of the three zigzag edges of WS₂ (**Fig. 4g**).

Outlook

We demonstrate the versatility of our synthesis method by creating large-scale, uniform HBCs with precisely tuned molecular unit cells, distinct from the conventional hetero-bilayers, as illustrated in **Fig. 4h** (solid dots). In particular, we synthesize MePDI lattice (**2**) with a quasi-four-fold geometry and a unit cell size of $\sim 3 \text{ nm}^2$, which is comparable to a MoS₂/WS₂ moiré unit cell, with an approximately 10° twist angle. Extending our approach to other molecular units—shown to produce even larger unit cells ($\sim 20 \text{ nm}^2$; open dots) with non-honeycomb geometries (e.g., square, rosette)^{17,51,52}—offers a powerful design strategy to access significantly dilute lattice or electronic regimes ($\sim 10^{12} \text{ unit cells/cm}^2$; shaded region in **Fig. 4h**) through direct synthesis. This opens new possibilities for fine-tuning the filling factors by “imprinting” large periodic potentials without requiring an interlayer twist. This hypothesis is supported by our *ab initio* calculations (**Fig. 3e**), showing that periodic potentials can indeed be imprinted by molecular crystals—an effect that could be amplified through charge modulation and doping. Furthermore, the anomalous, above-gap PL observed at low-temperatures, particularly in PDI-based HBCs, emphasizes the need to explore the exact relationship between the molecular lattice and the dielectric environment, including contributions from phonon states⁵³. The large-scale crystalline HBCs showcased here represent a significant leap forward in the design of molecule-based quantum materials, facilitating parameter tuning and the discovery of novel quantum behaviors.

References

1. Li, J. I. A., Taniguchi, T., Watanabe, K., Hone, J. & Dean, C. R. Excitonic superfluid phase in double bilayer graphene. *Nat. Phys.* **13**, 751–755 (2017).
2. Ma, L. *et al.* Strongly correlated excitonic insulator in atomic double layers. *Nature* **598**, 585–589 (2021).
3. Barré, E. *et al.* Optical absorption of interlayer excitons in transition-metal dichalcogenide heterostructures. *Science* **376**, 406–410 (2022).
4. Karni, O. *et al.* Structure of the moiré exciton captured by imaging its electron and hole. *Nature* **603**, 247–252 (2022).
5. Xiong, R. *et al.* Correlated insulator of excitons in WSe₂/WS₂ moiré superlattices. *Science* **380**, 860–864 (2023).
6. Ulman, K. & Quek, S. Y. Organic-2D Material Heterostructures: A Promising Platform for Exciton Condensation and Multiplication. *Nano Lett.* **21**, 8888–8894 (2021).
7. Corpinot, M. K. & Bučar, D.-K. A Practical Guide to the Design of Molecular Crystals. *Cryst. Growth Des.* **19**, 1426–1453 (2019).
8. Wasielewski, M. R. *et al.* Exploiting chemistry and molecular systems for quantum information science. *Nat. Rev. Chem.* **4**, 490–504 (2020).
9. Toninelli, C. *et al.* Single organic molecules for photonic quantum technologies. *Nat. Mater.* **20**, 1615–1628 (2021).
10. Li, T. *et al.* Continuous Mott transition in semiconductor moiré superlattices. *Nature* **597**, 350–354 (2021).
11. Cao, Y. *et al.* Unconventional superconductivity in magic-angle graphene superlattices. *Nature* **556**, 43–50 (2018).
12. Zhou, Y. *et al.* Bilayer Wigner crystals in a transition metal dichalcogenide heterostructure. *Nature* **595**, 48–52 (2021).
13. Li, H. *et al.* Imaging two-dimensional generalized Wigner crystals. *Nature* **597**, 650–654 (2021).
14. Tsui, Y.-C. *et al.* Direct observation of a magnetic-field-induced Wigner crystal. *Nature* **628**, 287–292 (2024).
15. He, D. *et al.* Two-dimensional quasi-freestanding molecular crystals for high-performance organic field-effect transistors. *Nat. Commun.* **5**, 5162 (2014).
16. Zhao, H. *et al.* Strong optical response and light emission from a monolayer molecular crystal. *Nat. Commun.* **10**, 5589 (2019).
17. Dong, J. *et al.* Free-standing homochiral 2D monolayers by exfoliation of molecular crystals. *Nature* **602**, 606–611 (2022).
18. Davydov, A. S. The Theory of Molecular Excitons. *Sov. Phys. Usp* **7**, 393–448 (1964).
19. Liu, X. *et al.* Photoresponse of an Organic Semiconductor/Two-Dimensional Transition Metal Dichalcogenide Heterojunction. *Nano Lett.* **17**, 3176–3181 (2017).
20. Cui, X. *et al.* Realizing nearly-free-electron like conduction band in a molecular film through mediating intermolecular van der Waals interactions. *Nat. Commun.* **10**, 3374 (2019).
21. Rijal, K. *et al.* Nanoscale Periodic Trapping Sites for Interlayer Excitons Built by Deformable Molecular Crystal on 2D Crystal. *ACS Nano* **17**, 7775–7786 (2023).
22. Wang, Q. H. & Hersam, M. C. Room-temperature molecular-resolution characterization of self-assembled organic monolayers on epitaxial graphene. *Nat. Chem.* **1**, 206–211 (2009).

23. Liu, X. *et al.* Self-assembly of electronically abrupt borophene/organic lateral heterostructures. *Sci. Adv.* **3**, e1602356 (2024).
24. Amsterdam, S. H. *et al.* Tailoring the Optical Response of Pentacene Thin Films via Templated Growth on Hexagonal Boron Nitride. *J. Phys. Chem. Lett.* **12**, 26–31 (2021).
25. Koo, S. *et al.* Extraordinary Photostability and Davydov Splitting in BN-Sandwiched Single-Layer Tetracene Molecular Crystals. *Nano Lett.* **21**, 6600–6608 (2021).
26. Kim, D. *et al.* In-plane and out-of-plane excitonic coupling in 2D molecular crystals. *Nat. Commun.* **14**, 2736 (2023).
27. Tsiper, E. V. & Soos, Z. G. Charge redistribution and polarization energy of organic molecular crystals. *Phys. Rev. B* **64**, 195124 (2001).
28. Kang, K. *et al.* High-mobility three-atom-thick semiconducting films with wafer-scale homogeneity. *Nature* **520**, 656–660 (2015).
29. Yang, H. *et al.* STM imaging, spectroscopy and manipulation of a self-assembled PTCDI monolayer on epitaxial graphene. *Phys. Chem. Chem. Phys.* **15**, 4939–4946 (2013).
30. Ludwig, C., Gompf, B., Petersen, J., Strohmaier, R. & Eisenmenger, W. STM investigations of PTCDA and PTCDI on graphite and MoS₂. A systematic study of epitaxy and STM image contrast. *Z. Physik B Condensed Matter* **93**, 365–373 (1994).
31. Hybertsen, M. S. & Louie, S. G. Electron correlation in semiconductors and insulators: Band gaps and quasiparticle energies. *Phys. Rev. B* **34**, 5390–5413 (1986).
32. Rohlfing, M. & Louie, S. G. Electron-hole excitations and optical spectra from first principles. *Phys. Rev. B* **62**, 4927 (2000).
33. Deslippe, J., Samsonidze, G., Jain, M., Cohen, M. L. & Louie, S. G. Coulomb-hole summations and energies for GW calculations with limited number of empty orbitals: A modified static remainder approach. *Phys. Rev. B* **87**, 165124 (2013).
34. Park, S. *et al.* Type-I Energy Level Alignment at the PTCDA—Monolayer MoS₂ Interface Promotes Resonance Energy Transfer and Luminescence Enhancement. *Adv. Sci.* **8**, 2100215 (2021).
35. Kobayashi, Y. *et al.* Growth and Optical Properties of High-Quality Monolayer WS₂ on Graphite. *ACS Nano* **9**, 4056–4063 (2015).
36. Ling, X. *et al.* Raman enhancement effect on two-dimensional layered materials: Graphene, h-BN and MoS₂. *Nano Lett.* **14**, 3033–3040 (2014).
37. Scharl, T. *et al.* Noncovalent Liquid Phase Functionalization of 2H-WS₂ with PDI: An Energy Conversion Platform with Long-Lived Charge Separation. *J. Am. Chem. Soc.* **144**, 5834–5840 (2022).
38. Müller, M., Paulheim, A., Eisfeld, A. & Sokolowski, M. Finite size line broadening and superradiance of optical transitions in two dimensional long-range ordered molecular aggregates. *J. Chem. Phys.* **139**, 044302 (2013).
39. Eisfeld, A., Marquardt, C., Paulheim, A. & Sokolowski, M. Superradiance from Two Dimensional Brick-Wall Aggregates of Dye Molecules: The Role of Size and Shape for the Temperature Dependence. *Phys. Rev. Lett.* **119**, 097402 (2017).
40. Peter, Y. U. & Cardona, M. *Fundamentals of Semiconductors: Physics and Materials Properties.* (Springer, 2010).
41. Kobitski, Y., Scholz, R., Zahn, T. & Wagner, P. Time-resolved photoluminescence study of excitons in α -PTCDA as a function of temperature. *Phys. Rev. B* **68**, 155201 (2003).
42. D’Andrade, B. & Forrest, S. R. Formation of triplet excimers and dimers in amorphous organic thin films and light emitting devices. *Chem. Phys.* **286**, 321–335 (2003).

43. Gangilenka, V. R. *et al.* Selective excitation of exciton transitions in PTCDA crystals and films. *Phys Rev B* **81**, 155208 (2010).
44. Ud Din, N. & Liu, Z.-F. Anisotropy of the Optical Properties of Pentacene:Black Phosphorus Interfaces. *J. Phys. Chem. C* **126**, 20694–20701 (2022).
45. Sharifzadeh, S., Darancet, P., Kronik, L. & Neaton, J. B. Low-Energy Charge-Transfer Excitons in Organic Solids from First-Principles: The Case of Pentacene. *J. Phys. Chem. Lett.* **4**, 2197–2201 (2013).
46. Sharifzadeh, S. *et al.* Relating the Physical Structure and Optoelectronic Function of Crystalline TIPS-Pentacene. *Adv. Funct. Mater.* **25**, 2038–2046 (2015).
47. Cheng, C.-H., Cordovilla Leon, D., Li, Z., Litvak, E. & Deotare, P. B. Energy Transport of Hybrid Charge-Transfer Excitons. *ACS Nano* **14**, 10462–10470 (2020).
48. Zhu, T. *et al.* Highly mobile charge-transfer excitons in two-dimensional WS₂/tetracene heterostructures. *Sci. Adv.* **4**, eaao3104 (2018).
49. Bennecke, W. *et al.* Hybrid Frenkel-Wannier excitons facilitate ultrafast energy transfer at a 2D-organic interface. *arXiv preprint arXiv:2411.14993* (2024).
50. Wu, F., Lovorn, T., Tutuc, E. & MacDonald, A. H. Hubbard Model Physics in Transition Metal Dichalcogenide Moiré Bands. *Phys. Rev. Lett.* **121**, 26402 (2018).
51. Liang, B. *et al.* Optimal acceleration voltage for near-atomic resolution imaging of layer-stacked 2D polymer thin films. *Nat. Commun.* **13**, 3948 (2022).
52. Kharel, P. *et al.* Atomic-Resolution Imaging of Small Organic Molecules on Graphene. *Nano Lett.* **22**, 3628–3635 (2022).
53. Alvertis, A. M., Haber, J. B., Engel, E. A., Sharifzadeh, S. & Neaton, J. B. Phonon-Induced Localization of Excitons in Molecular Crystals from First Principles. *Phys. Rev. Lett.* **130**, 86401 (2023).
54. Liu, Z.-F., da Jornada, F. H., Louie, S. G. & Neaton, J. B. Accelerating GW-Based Energy Level Alignment Calculations for Molecule–Metal Interfaces Using a Substrate Screening Approach. *J. Chem. Theory Comput.* **15**, 4218–4227 (2019).

Acknowledgements: We thank A. J. Mannix and M. Lee for helpful discussions regarding scanning probe and optical measurements, respectively. We also thank Z. Liu, O. Adeniran and S. Sharifzadeh for helpful discussions and for providing the scripts used for the calculations.

Funding: Primary funding for this work comes from the Air Force Office of Scientific Research (FA9550-21-1-0323) and the MURI project (FA9550-18-1-0480). Additional funding was provided by the Office of Naval Research (N000142212841) and Samsung Advanced Institute of Technology. T.C. acknowledges the Kadanoff-Rice Postdoctoral Fellowship from the National Science Foundation (NSF) Materials Research Science and Engineering Center (MRSEC) under grant no. DMR-2011854. F.M. acknowledges support by the NSF Graduate Research Fellowship Program under grant no. DGE-1746045. Work performed at the Center for Nanoscale Materials, a U.S. Department of Energy Office of Science User Facility, was supported by the U.S. DOE, Office of Basic Energy Sciences, under contract no. DE-AC02-06CH11357. The calculation in this work are primarily supported by the Center for Computational Study of Excited-State Phenomena in Energy Materials (C2SEPEM), funded by the U.S. DOE under contract no. DE-FG02-07ER46405. The Theory of Materials FWP at LBNL, funded by the DOE under contract no. DE-AC02-05CH11231, supported the development of the theories and models. Computational resources are provided by the National Energy Research Scientific Computing Center (NERSC). P.K. acknowledges financial support from the Swiss National Science Foundation. A.R. and the STEM imaging at the Cornell Center for Materials Research are supported by the NSF-MRSEC grant no. DMF-1719875. The Thermo Fisher Spectra 300 X-CFEG was acquired with support from PARADIM, an NSF MIP (DMR-2039380) and Cornell University.

Author Contributions: T.C., F.M., and J.P. conceived the project. A.C. performed the ab-initio calculations and the analysis of the excited states under the supervision of J.B.N. T.C. and F.M. developed the large-scale synthesis and cross-polarized imaging of HBCs. C.L. helped with the synthesis. T.C. conducted the PL imaging with assistance from Z.N. T.C. and P.K. performed the cryogenic optical measurements. N.G. and F.M. conducted the STM imaging. A.R. performed the STEM imaging. M.G. conducted supplementary electrochemical measurements. T.C. analyzed the experimental data and performed numerical calculations. T.C. and J.P. wrote the manuscript, with input from all authors.

Competing interests: The authors declare no competing financial interests.

Data and materials availability: All data are reported in the main text and supplementary materials. The code used to fold/map/add the noninteracting polarizability matrices was first proposed by Liu *et al.*⁵⁴ and is available upon request. The code used to decompose the excited states was first proposed by Ud Din *et al.*⁴⁴ and is available upon request. The code used to compute the electron-hole correlation function was first proposed in Sharifzadeh *et al.*⁴⁵ and is available upon request. The BerkeleyGW package used for GW-BSE calculations is a free, open source package available at berkeleygw.org. The code used to plot the band projections is available at pymtgen.electronic_structure_package.

Methods

Large-scale synthesis of HBCs. Inch-scale uniform and monolayer TMDs (MoS_2 , WS_2) were synthesized on both $\text{SiO}_2/\text{Si}(100)$ (University Wafer, Inc., 300 nm wet thermal SiO_2 , SSP) and fused Silica (University Wafer, Inc., 500 μm , DSP) wafers through metal-organic chemical vapor deposition (MOCVD) adapted from a previously reported protocol²⁸. The MOCVD conditions were optimized to produce high-quality, monolayer TMDs with morphological characteristics suitable for molecular monolayer deposition and wide-field optical imaging. These characteristics include large single-crystal domain size (D) for both laterally-stitched, continuous polycrystal MoS_2 grains (D~20 μm) and isolated WS_2 triangles (D~50–250 μm). To begin, commercially available high purity (~98–99 w%) powdered molecular precursor (Sigma Aldrich, PDI, PTCDA, MePDI, C5-PDI, C8-PDI, PhPDI, and THPP) was loaded into a hot-walled quartz tube physical vapor deposition (PVD) reactor without further purification. Prior to growth, the as-grown TMD samples were thoroughly rinsed with HPLC grade methanol and isopropyl alcohol, dried under nitrogen flow, and promptly positioned (within ~2 min) alongside the molecular precursor in the reactor, which was subsequently pumped down. The precise positioning of the substrate relative to the molecular precursor is critical to ensure self-limited monolayer molecular deposition and prevent multilayered or bulk molecular crystal formation. The PVD reactor was then sequentially flushed with ultrahigh purity nitrogen (N_2) gas (flow rate: 1000 standard cubic centimeters per minute or sccm) and evacuated to a base pressure of $\sim 6 \times 10^{-4}$ torr. Once the base pressure was reached, the temperature of the furnace was quickly ramped to 120 °C to remove completely the moisture and low-boiling organic impurities under a 200 sccm N_2 flow for ~2–3 hours. For certain HBC synthesis, multiple full PVD cycles (i.e., time required to raise the temperature of the furnace, maintain that temperature for a specific duration of time, and cool down to room temperature) were performed to achieve complete molecular monolayer coverage. The specific reaction conditions for different HBCs are provided in Supplementary Table 3.

Scanning probe microscopy. Topography and thickness of the as-grown HBC samples were determined by state-of-the-art atomic force microscopy (AFM) (Cypher ES AFM equipped with blueDrive™) using a fast-scanning high-frequency silicon probe (FS-1500AUD; tip radius 10 nm) in ambient conditions. For scanning tunneling microscopy (STM) measurements in ultrahigh vacuum (UHV) conditions, as-grown continuous HBC samples were first water-delaminated from the SiO_2/Si growth substrates and then transferred on to Au(111)-coated mica substrates (Phasis) for imaging at room temperature. Measurements utilized a commercial variable temperature STM (VT Scienta Omicron) operating at a base pressure of 5×10^{-11} mbar. Imaging utilized electrochemically sharpened tungsten tips. Samples were annealed overnight in a UHV preparation chamber at approximately 100 °C to drive off mostly water and any physisorbed contamination. The preparation chamber is connected to the analysis chamber, so the samples remained in situ between annealing and imaging. Sample biases (V) and tunneling currents (I) for these images are $V = -800$ mV; $I = 50$ pA (PDI), $V = -1$ V; $I = 100$ pA (PTCDA), and $V = +2$ V; $I = 100$ pA (MePDI).

Aberration corrected scanning transmission electron microscopy (ac-STEM). Cross-sectional HBC samples were prepared using a Thermo Fisher Helios G4 UX Focused Ion Beam (FIB) with protective layers of carbon and platinum deposited by both the electron and Ga ion beam. The cross-section was cut at a 90° angle from the sample and initially milled at an ion beam voltage of 30 kV. Final milling was done at 5 kV. The samples were then imaged in an aberration-corrected Thermo Fisher Scientific Spectra 300 X-FEG STEM at 300 kV with a probe semi-convergence angle of 30 mrad. The integrated differential phase contrast (iDPC) image (Fig. 1c) has been found to represent the sample's projected electrostatic potential⁵⁵, and therefore its contrast scales weakly with atomic number⁵⁵⁻⁵⁷. For this reason, compared to high-angle annular dark-field (HAADF) imaging, iDPC image is able to detect simultaneously both the light molecular crystal layer and heavier TMD layer with high spatial resolution. The iDPC image also has better dose efficiency and less noise than the HAADF image due to utilizing a greater fraction of the available electrons, allowing us to capture the beam-sensitive molecular crystal layer; however, we were not able to resolve the internal details in the molecular crystal layer due to radiation damage from the electron beam⁵⁶. Raw data for the iDPC image is collected on an annular detector split into four equal angular segments covering portions of the bright field disk and low angle scattering region of the diffraction pattern. In order to create the iDPC image, the signals from both pairs of opposite detector segments are first subtracted to form a vector DPC image. The DPC images are then integrated in Fourier space following a method⁵⁶ to form an iDPC image. A high-pass filter was applied to the iDPC image to remove the slowly varying carbon contamination background.

Wide-field PL microscopy. Temperature dependent polarized PL measurements were carried out in our homebuilt hyperspectral PL microscope coupled with a closed-loop Helium cryostat (Montana) with variable temperature from 4K to room temperature. We utilized a fiber-coupled 532 nm continuous wave laser with output power 30 mW as excitation that was passed through a linear polarizer, a half waveplate (or a quarter waveplate), and a long-pass 90:10 dichroic beam splitter, and normally shone on to the sample with a strain-free 20× objective (NA = 0.5). The emitted light was directed through an analyzer and a pair of tunable filters (Semrock Edge) and then collected by a CMOS camera (pco.edge) with a spectral resolution of 10 meV. Angle-dependent PL at 4 K was measured by rotating the wave-plate while maintaining the incident co-linear polarization.

Confocal PL spectroscopy. The confocal PL experiments were performed in a cryostat (Montana) with variable temperature from 4 K to room temperature. A 532 nm laser was used as excitation source, from which a power of 50 μ W was focused to about 1 μ m² onto the sample using a 40× objective (NA = 0.6). A long pass filter removed the laser light from the reflected beam. The collected emission signal was sent to a spectrometer and detected on a liquid nitrogen cooled CCD camera (Princeton Instruments) with a spectral resolution of 1 meV. For temperature-dependent PL measurement, the excitation beam was circularly polarized. To record the angle-dependent PL,

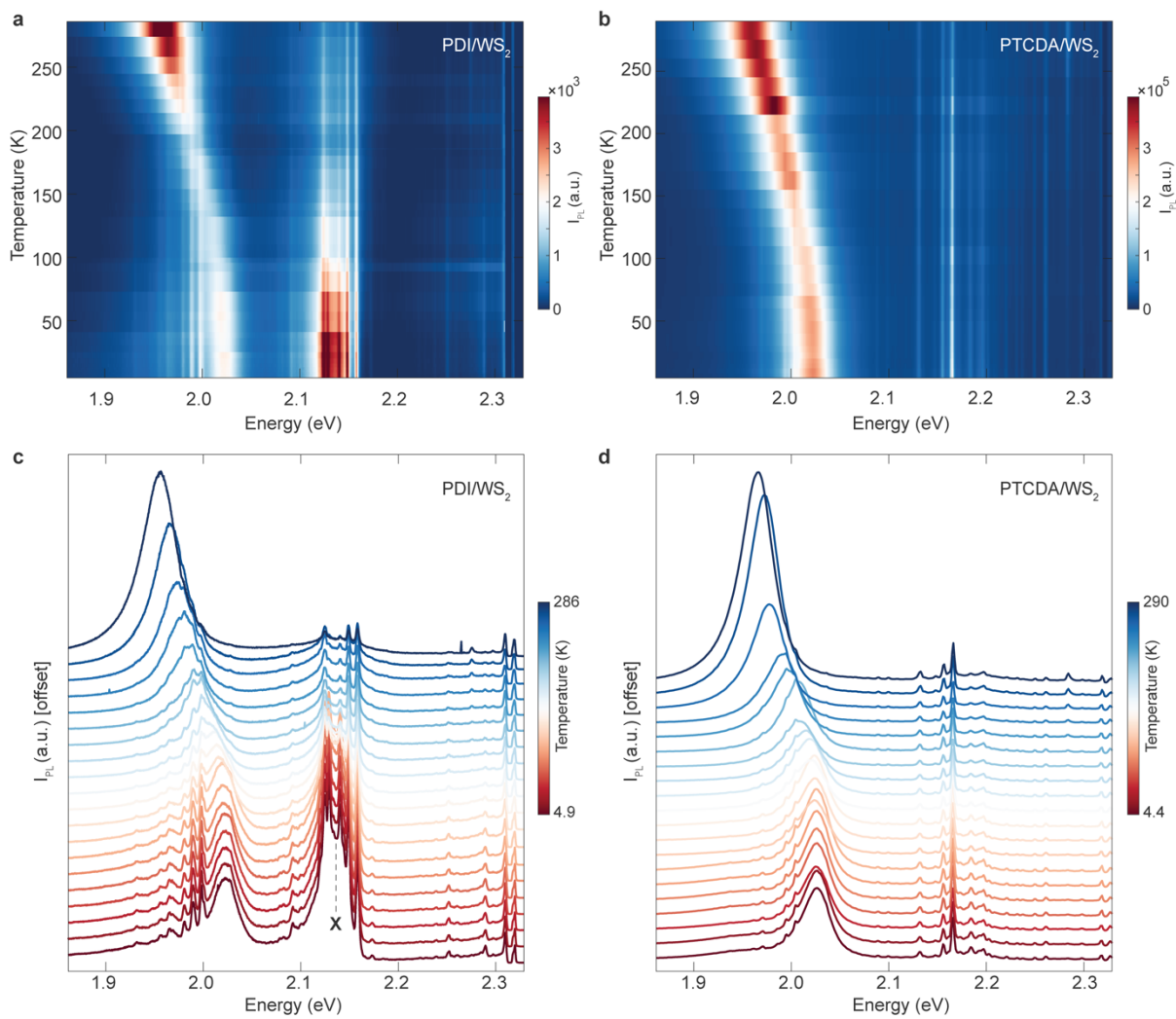
two aligned linear polarizers were placed in the excitation and detection paths, while a half wave plate common to both paths was rotated.

Wide-field reflectance microscopy. Wide-field cross-polarized differential reflectance or reflection contrast ($\Delta R/R$) images and spectra were acquired in our homebuilt hyperspectral microscope. First, a broadband white light (Xenon lamp, 400–700 nm) was passed through a monochromator and then coupled to a multimode fiber. The fiber-coupled light was passed through a linear polarizer and a 90:10 dichroic beam splitter and shone on to the sample mounted on a rotatable stage with a strain-free 20 \times objective lens (NA = 0.5). The reflected light was first passed through the beam splitter and then an analyzing polarizer rotated at a small angle ($\sim 3^\circ$ – 5°) from the cross-polarizer geometry. This nearly orthogonal polarizer configuration significantly improves the signal to noise ratio by suppressing the isotropic response from the substrate (SiO₂ or TMD/SiO₂) without notably diminishing the anisotropic response from the molecular domain⁵¹. Reflected signals were detected by an electron-multiplying CCD camera (Andor iXon+). This imaging technique provides simultaneous assessment of the material’s morphology and macroscopic optical anisotropy across a large field-of-view ($\sim 0.5 \times 0.5$ mm²). The low-power (~ 0.03 mW/mm²) and rapid (50–100 ms/frame) imaging prevents the soft molecular crystals against beam-induced damage and photobleaching.

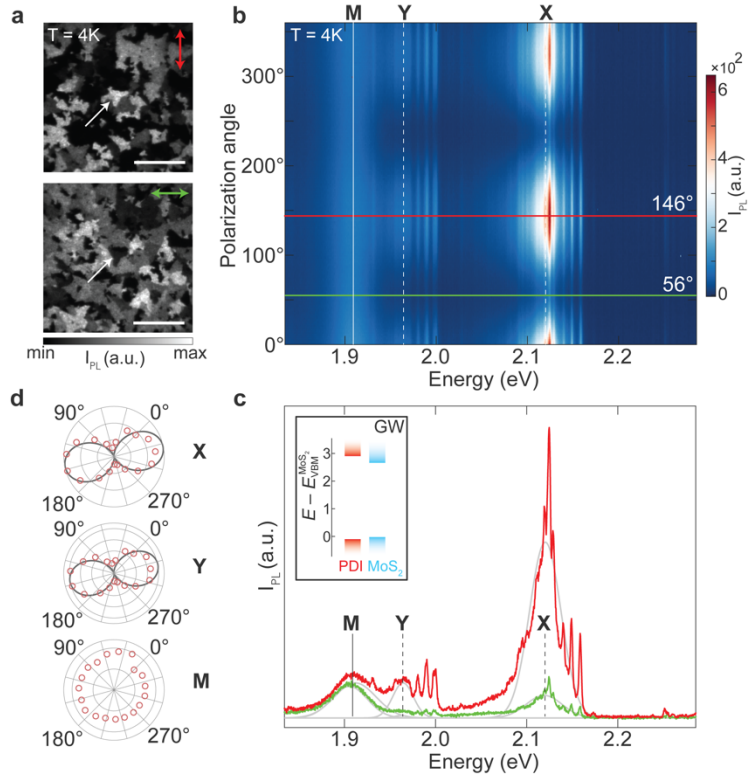
Ab initio GW-BSE calculations. The ab initio GW and GW-Bethe-Salpeter equation (GW-BSE) approach is a state-of-the-art method for the accurate prediction of one- and two-particle excitations, respectively. Central to this approach is the computation of the dielectric function, which encodes how the many-electron systems screens charged and neutral excitations. Our GW-BSE calculations start with density functional theory (DFT) calculations performed with the Quantum Espresso package^{59,62} which uses a plane-wave basis set and norm-conserving ONCVSP pseudopotentials^{61,62}. We use a Perdew Burke and Ernzerhof (PBE) functional⁶³ with a vdw-Grimme-D3 correction⁶⁴ for all DFT calculations. Our one-shot G_0W_0 calculations^{65–67} using a PBE starting point are performed with the BerkeleyGW code^{33,68}, using the Hybertsen-Louie generalized plasmon pole for the frequency dependence of the dielectric function⁶⁷, the shifted-grid approach to deal with the divergence of the Coulomb interaction at $q = 0$ ³³, a slab truncation of the Coulomb interaction⁶⁹, and the static remainder for the self-energy calculation to speed up the convergence with respect to unoccupied states³³. To reduce the computational cost, and in particular the expense associated with computing the interface dielectric function, we apply a substrate screening GW approach⁵⁴. The optical absorption spectra and excitonic properties are computed using the GW-BSE approach within the Tamm-Dancoff approximation, as implemented in the BerkeleyGW package^{33,68}.

Methods References

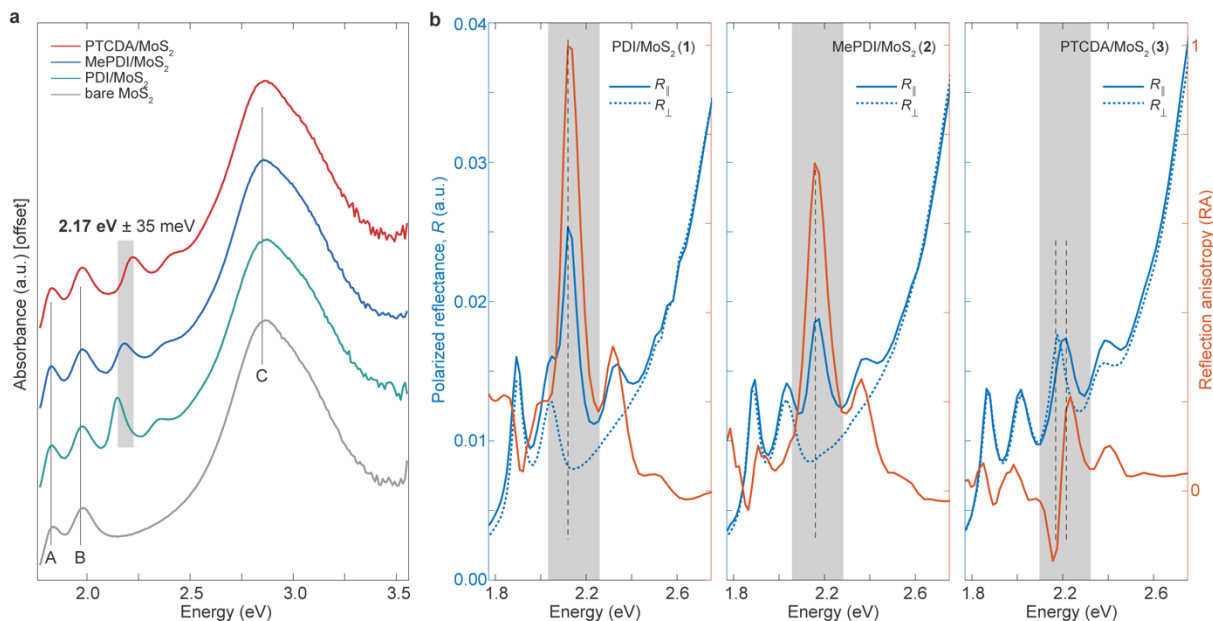
55. Close, R., Chen, Z., Shibata, N. & Findlay, S. D. Towards quantitative, atomic-resolution reconstruction of the electrostatic potential via differential phase contrast using electrons. *Ultramicroscopy* **159**, 124–137 (2015).
56. Lazić, I., Bosch, E. G. T. & Lazar, S. Phase contrast STEM for thin samples: Integrated differential phase contrast. *Ultramicroscopy* **160**, 265–280 (2016).
57. Yücelen, E., Lazić, I. & Bosch, E. G. T. Phase contrast scanning transmission electron microscopy imaging of light and heavy atoms at the limit of contrast and resolution. *Sci. Rep.* **8**, 2676 (2018).
58. Gallagher, P. *et al.* Optical Imaging and Spectroscopic Characterization of Self-Assembled Environmental Adsorbates on Graphene. *Nano Lett.* **18**, 2603–2608 (2018).
59. Giannozzi, P. *et al.* QUANTUM ESPRESSO: A modular and open-source software project for quantum simulations of materials. *J. Phys. Condens. Matter* **21**, 395502 (2009).
60. Giannozzi, P. *et al.* Advanced capabilities for materials modelling with Quantum ESPRESSO. *J. Phys. Condens. Matter* **29**, 465901 (2017).
61. Hamann, D. R. Optimized norm-conserving Vanderbilt pseudopotentials. *Phys. Rev. B* **88**, 085117 (2013).
62. Schlipf, M. & Gygi, F. Optimization algorithm for the generation of ONCV pseudopotentials. *Comput. Phys. Commun.* **196**, 36–44 (2015).
63. Perdew, J. P., Burke, K. & Ernzerhof, M. Generalized Gradient Approximation Made Simple. *Phys. Rev. Lett.* **78**, 1396 (1997).
64. Grimme, S., Antony, J., Ehrlich, S. & Krieg, H. A consistent and accurate ab initio parametrization of density functional dispersion correction (DFT-D) for the 94 elements H-Pu. *J. Chem. Phys.* **132**, 154104 (2010).
65. Hedin, L. New Method for Calculating the One-Particle Green's Function with Application to the Electron-Gas Problem. *Phys. Rev.* **139**, A796 (1965).
66. Strinati, G., Mattausch, H. J. & Hanke, W. Dynamical Aspects of Correlation Corrections in a Covalent Crystal. *Phys. Rev. B* **25**, 2867 (1982).
67. Hybertsen, M. S. & Louie, S. G. Electron Correlation in Semiconductors and Insulators: Band Gaps and Quasiparticle Energies. *Phys. Rev. B* **34**, 5390 (1986).
68. Deslippe, J. *et al.* BerkeleyGW: A massively parallel computer package for the calculation of the quasiparticle and optical properties of materials and nanostructures. *Comput. Phys. Commun.* **183**, 1269–1289 (2012).
69. Ismail-Beigi, S. Truncation of periodic image interactions for confined systems. *Phys. Rev. B* **73**, 233103 (2006).



Extended Data Fig. 1. Temperature-dependent PL spectra. Temperature-dependent polarized PL maps of single-crystalline domains of PDI/WS₂ (a) and PTCDA/WS₂ (b). Selected line spectra highlighting PL signal X (c; dotted dashed line) in PDI/WS₂, while no such signal is observed in PTCDA/WS₂ (d).



Extended Data Fig. 2. Low-temperature polarized PL from PDI/MoS₂. (a) Low-temperature wide-field PL images of polycrystalline PDI/MoS₂ at 2.12 eV at two orthogonal polarization directions indicated as double-sided red and green arrows. White arrows highlight a single-crystalline PDI/MoS₂ domain. Scale: 40 μm . (b) Polarization angle-dependent confocal PL map from a single crystal PDI/MoS₂ domain at $T = 4\text{K}$, highlighting three peaks: X, Y by dashed white lines, and M by solid white line. (c) Selected PL spectra generated from the linecuts in (b) highlighting peaks X, Y, and M. *Inset*: GW-computed band alignment in PDI/MoS₂, showing a type-I interface. (d) Polar scatter plots for peaks X, Y, and W generated from (b), with overlaid cosine-squared fits for X and Y.



Extended Data Fig. 3. Room-temperature absorption/reflection spectra of HBCs. (a) Unpolarized UV-vis absorption spectra of PDI/MoS₂, PTCDA/MoS₂, and MePDI/MoS₂ on transparent (fused silica) substrates. Primary molecular absorption feature is highlighted by the grey boxed region. Bare MoS₂ spectrum is shown to identify A, B, and C exciton peaks of MoS₂. (b) Polarized reflectance spectra from single crystal domains of PDI/MoS₂ (1), MePDI/MoS₂ (2), and PTCDA/MoS₂ (3) for parallel (\parallel ; solid blue line) and perpendicular (\perp ; dotted blue line) alignment of each domain relative to the incident polarization direction. The reflection anisotropy (RA) spectra (orange line) are overlaid with raw data. The dashed black lines highlight the energies corresponding to the primary molecular features. The two closely spaced dotted black lines for (3) indicate the presence of Davydov doublets.

Supplementary Information

for

Molecular tuning of excitons and polarization anisotropy in hybrid bilayer crystals

Authors:

Tomojit Chowdhury^{1,2,10}, Aurélie Champagne^{3,4,10}, Fauzia Mujid¹, Patrick Knüppel⁵, Zehra Naqvi⁶,
Ce Liang⁶, Ariana Ray⁷, Mengyu Gao¹, David A. Muller⁷, Nathan Guisinger⁸, Kin Fai Mak⁵,
Jeffrey B. Neaton^{3,4,9}, & Jiwoong Park^{1,2,6*}

Affiliations:

¹Department of Chemistry, University of Chicago, Chicago, IL, USA

²James Franck Institute, University of Chicago, Chicago, IL, USA

³Department of Physics, University of California, Berkeley, CA, USA

⁴Materials Science Division, Lawrence Berkeley National Laboratory, Berkeley, CA, USA

⁵Department of Physics, Cornell University, Ithaca, NY, USA

⁶Pritzker School of Molecular Engineering, University of Chicago, Chicago, IL, USA

⁷Department of Applied and Engineering Physics, Cornell University, Ithaca, NY, USA

⁸Center for Nanoscale Materials, Argonne National Laboratory, Lemont, IL, USA

⁹Kavli Energy Nanoscience Institute, University of California, Berkeley, CA, USA

¹⁰These authors contributed equally to this work

*corresponding author: jwpark@uchicago.edu

Table of Contents

Supplementary Discussion	4
Computational details	4
Analysis of the excited states in HBC	6
Generation of the electron isosurface maps	7
Estimation of misorientation angles	8
Estimation of dipolar anisotropy from a vector model	9
Method of PL data acquisition	10
Calculation of optical anisotropy	11
Photoluminescence anisotropy:	11
Reflection contrast and anisotropy:	11
Calculation of the thermal activation energy of exciton	11
Analysis of crystalline domain structures	12
Ionic gate spectroscopy	12
Calculation of lattice density and equivalent twist angle	12
Supplementary Figures	14
Supplementary Fig. 1. Morphology and topography of HBC	14
Supplementary Fig. 2. Molecular lattice structures	15
Supplementary Fig. 3. Estimation of misorientation angles (ξ)	16
Supplementary Fig. 4. STM characterization of MePDI lattice	17
Supplementary Fig. 5. Computed PDI/WS₂ supercell	18
Supplementary Fig. 6. Computed band structures of freestanding monolayers	19
Supplementary Fig. 7. Computed density of states and square of wavefunctions at K point	20
Supplementary Fig. 8. Electrochemical transport properties of PDI/WS₂	21
Supplementary Fig. 9. Home-built optical measurement systems	22
Supplementary Fig. 10. Identification of Raman modes of PDI/WS₂	23
Supplementary Fig. 11. Wide-range PL spectra of PDI/WS₂	24
Supplementary Fig. 12. Computed full absorption spectrum of PDI/WS₂	25
Supplementary Fig. 13. Computed electron isosurface map of WS₂ exciton	26
Supplementary Fig. 14. Computed vertical delocalization of hybrid exciton	27
Supplementary Fig. 15. Computed oscillator strengths of excitons in PDI/WS₂	28
Supplementary Fig. 16. Computed potential well depths in PDI/WS₂	29
Supplementary Fig. 17. Poly-crystalline HBC domain structure analysis	30

Supplementary Fig. 18. Vector model for dipolar anisotropy ($\Delta\mu$).....	31
Supplementary Fig. 19. Wafer-scale synthesis and characterization of perylene-based HBCs.	32
Supplementary Fig. 20. Synthesis and characterization of porphyrin-based HBCs.	33
Supplementary Fig. 21. Synthesis and characterization of PDI/graphene.	34
Supplementary Fig. 22. Synthesis and characterization of PDI/hBN.....	35
Supplementary Fig. 23. Single- and poly-crystal PDI domains on single-crystal WS₂.	36
Supplementary Tables.....	37
Supplementary Table 1. Experimental lattice parameters.	37
Supplementary Table 2. Computed lattice parameters.	38
Supplementary Table 3. Reaction conditions for different HBCs.....	39
Supplementary References	40

Supplementary Discussion

Computational details

The first step in our calculations consists in relaxing the in-plane lattice parameters and atomic coordinates of the WS₂ monolayer unit cell, starting from the experimental lattice parameters. To perform the DFT calculations, we use the Perdew Burke and Ernzerhof (PBE) functional¹ with a vdW-Grimme-D3 correction² and the Quantum Espresso package^{3,4}, which uses a plane-wave basis set and norm-conserving ONSVSP pseudopotentials^{5,6} from the PseudoDojo. We use a cut-off energy of 125 Ry and include a vacuum of $\sim 17\text{\AA}$ along the out-of-plane direction, to avoid spurious interactions with repeated unit cells. A uniform $24\times 24\times 1$ k-grid is used in the relaxation calculation. The resulting lattice constant is 3.16\AA for WS₂.

After the TMD unit cell relaxation, we build a $4\times 8\times 1$ supercell and place the one-atom-thick PDI layer onto the TMD substrate. The interface supercell is 30\AA along the out-of-plane direction, corresponding to $\sim 23\text{\AA}$ of vacuum. The $4\times 8\times 1$ supercell is chosen because it is closest to being commensurate with the PDI unit cell, requiring just a modest stretching of the PDI layer, as small as $\sim 2\%$; we verified that this stretching does not affect the electronic properties of the PDI layer. While keeping the atomic positions in the TMD layer fixed to ensure the exactness of the subsequent reciprocal-space folding of the noninteracting polarizability, the coordinates of the atoms within the molecular layer are relaxed along the three directions. A resulting interlayer distance of 3.43\AA is found, in good agreement with interlayer distances reported for similar systems⁷. The supercell relaxation is performed using DFT-PBE with vdW-Grimme-D3 correction², a cut-off energy of 70 Ry, and a uniform $6\times 3\times 1$ k-grid. The interface Brillouin zone (BZ) is obtained by dividing the reciprocal lattice vectors of the TMD monolayer respectively by 4, 8 and 1. The high-symmetry path used in the calculation of the interface bandstructure include the Γ (0,0,0), M (0.5,0,0), and K ($1/3, 2/3, 0$) k-points. Self-consistent calculations with a same cut-off energy and k-grid are performed and the results are post-processed using pp.x in Quantum Espresso to obtain the electronic wavefunction at K and the $V_z(x, y)$ potential (bare + Hartree).

The GW calculations⁸⁻¹⁰ are performed with the BerkeleyGW code^{11,12}—starting from Kohn-Sham eigenstates computed from the PBE functional¹ with a vdW-Grimme-D3 correction²—using the Hybertsen-Louie generalized plasmon pole (GPP) for the frequency dependence of the dielectric function¹⁰, the shifted-grid approach to deal with the divergence of the Coulomb interaction at $q = 0$ ¹², the slab Coulomb truncation¹³, and the static remainder in the self-energy

calculation to improve convergence ¹². We neglect spin-orbit coupling to reduce computational cost, which is known to cause a 0.4 and 0.03 eV splitting for WS₂ in the valence and conduction band, respectively ¹⁴. To reduce the computational cost of conventional GW, in particular for such large interface cell, we use the substrate screening GW approach ¹⁵ and keep all GW calculations at the G₀W₀ level.

For the calculation of the noninteracting polarizability of the substrate unit cell, χ_{sub}^0 , we use a q-mesh of 24×24×1, a 5 Ry dielectric cutoff, and 400 bands in the Coulomb-hole summation. For the treatment of the q→0 limit, we use 18 bands on a shifted q-grid. For the calculation of the noninteracting polarizability of the adsorbed molecular layer, χ_{mol}^0 , we use a simulation cell with the same a and b lattice constants as the interface but a halved c parameter of 15 Å. We use a q-mesh of 6×3×1, a 5 Ry dielectric cutoff, and 6,400 bands in the Coulomb-hole summation. For the treatment of the q→0 limit, we use 288 bands on a shifted q-grid. Following reference ¹⁵, χ_{sub}^0 is folded in the reciprocal space to a 4×8×1 supercell, and χ_{mol}^0 is mapped in the real space to the interface simulation cell. The interface noninteracting polarizability, χ_{total}^0 , is approximated as $\chi_{\text{total}}^0 = \chi_{\text{sub}}^0 + \chi_{\text{mol}}^0$ at each q-point. The interface polarizability matrix is then inverted to generate the dielectric function in the interface simulation cell, and the self-energy correction is computed within the GW approach, using a k-mesh of 6×3×1, a 5 Ry dielectric cutoff, and 12,800 bands in the Coulomb-hole summation.

The neutral excitations including electron-hole interactions and the optical response of the TMD, the molecular adsorbate, and the interface are computed using the ab initio GW plus Bethe-Salpeter equation (GW-BSE) approach as implemented in the Berkeley GW package ^{11,12}. The BSE matrix elements of the TMD substrate are computed on a uniform 24×24×1 coarse k-grid, then interpolated onto a 192×192×1 fine k-grid, with 2 valence and 4 conduction bands. The BSE matrix elements of the molecular adsorbate layer are computed on a uniform 6×3×1 coarse k-grid, then interpolated onto a 48×24×1 fine k-grid, with 12 valence and 12 conduction bands. The BSE matrix elements of the interface are computed on a uniform 6×3×1 coarse k-grid, then interpolated onto a 12×6×1 fine k-grid, with 20 valence and 20 conduction bands. Due to computational cost constraints, we restrict ourselves to relatively coarse k-grids and small number of unoccupied bands in the calculation of the electron-hole kernel, which results in optical spectra converged within 100 meV for energies below 2.7 eV.

Analysis of the excited states in HBC

The exciton binding energy, E_b , for a homogeneous system is defined as the difference between the independent particle energy gap, E_g , and exciton energy, Ω^S . For HBC, the independent particle energy gaps are obtained by projecting the combined states onto the molecular orbitals and TMD bands. For hybrid excitons, i.e., with a significant contribution from both molecular and TMD layers, the energy gap (and hence exciton binding) is not well defined. Hence, we use the attractive electron-hole Coulomb interaction as a measure of the energetic stabilization of the excitons¹⁶. The electron-hole attractive kernel K_{e-h} is defined as:

$$K_{e-h} = \langle S | \hat{K} | S \rangle = \sum_{cvk} (E_{ck} - E_{vk}) |A_{cvk}|^2 - \Omega^S$$

A large value of K_{e-h} thus corresponds to a strong electron-hole binding while small value corresponds to a weaker electron-hole interaction.

Next, using the computational scheme developed previously¹⁷, we decompose the HBC excited states into different contributions (i.e., molecular, TMD, and interlayer). For each excited state (eigen vector) of the HBC, we have:

$$\psi(r_e, r_h) = \sum_{v \in total}^{occ} \sum_{c \in total}^{unocc} A_{vc} \phi_v^*(r_h) \phi_c(r_e)$$

where r_e (r_h) is the electron (hole) coordinate, v (c) runs over all occupied (unoccupied) Kohn-Sham orbitals of the interface, ϕ_v (ϕ_c), and A_{vc} 's are the expansion coefficients. Each interface orbital can be linearly expanded in terms of orbitals of the molecule and substrate in their freestanding phase:

$$\phi_v^*(r_h) = \sum_{i \in mol}^{occ} C_{vi}^* \phi_i^*(r_h) + \sum_{j \in TMD}^{occ} C_{vj}^* \phi_j^*(r_h)$$

$$\phi_c^*(r_e) = \sum_{a \in \text{mol}}^{\text{unocc}} C_{ca}^* \phi_a^*(r_e) + \sum_{b \in \text{TMD}}^{\text{unocc}} C_{cb}^* \phi_b^*(r_e)$$

where C 's are the expansion coefficients of the freestanding molecular and TMD layers. Now, combining the above two expressions, we find:

$$\begin{aligned} \psi(r_e, r_h) = & \sum_{v \in \text{total}}^{\text{occ}} \sum_{c \in \text{total}}^{\text{unocc}} A_{vc} \sum_{i \in \text{mol}}^{\text{occ}} \sum_{a \in \text{mol}}^{\text{unocc}} C_{vi}^* C_{ca} \phi_i^*(r_h) \phi_a(r_e) \\ & + \sum_{v \in \text{total}}^{\text{occ}} \sum_{c \in \text{total}}^{\text{unocc}} A_{vc} \sum_{j \in \text{TMD}}^{\text{occ}} \sum_{b \in \text{TMD}}^{\text{unocc}} C_{vj}^* C_{cb} \phi_j^*(r_h) \phi_b(r_e) \\ & + \sum_{v \in \text{total}}^{\text{occ}} \sum_{c \in \text{total}}^{\text{unocc}} A_{vc} \sum_{i \in \text{mol}}^{\text{occ}} \sum_{b \in \text{TMD}}^{\text{unocc}} C_{vi}^* C_{cb} \phi_i^*(r_h) \phi_b(r_e) \\ & + \sum_{v \in \text{total}}^{\text{occ}} \sum_{c \in \text{total}}^{\text{unocc}} A_{vc} \sum_{j \in \text{TMD}}^{\text{occ}} \sum_{a \in \text{mol}}^{\text{unocc}} C_{vj}^* C_{ca} \phi_j^*(r_h) \phi_a(r_e) \end{aligned}$$

On the right hand side, the first, second, third, and fourth terms indicate an intralayer molecular layer exciton (i.e., electron and hole in the molecular layer), an intralayer TMD exciton (i.e., electron and hole in the TMD layer), a high-energy interlayer exciton (i.e., electron in the TMD layer and hole in molecular layer), and a low-energy interlayer exciton (i.e., electron in the molecular layer and hole in TMD layer), respectively. This decomposition scheme, by plotting the weighted expansion coefficients as a function of energy, is used to generate Fig. 3a and Supplementary Fig. 11.

Generation of the electron isosurface maps

For a given excited state wavefunction, the electron-hole correlation function, $\mathcal{F}_S(r)$, is expressed as the following^{18,19}:

$$\mathcal{F}_S(r) = \int_{\Omega}^{\text{all space}} d^3 r_h |\psi_S(r_e = r_h + r, r_h)|^2$$

which describes the probability of finding electron and hole separated by a vector $r = r_e - r_h$. $\psi_S(r_e, r_h)$ is the normalized electron-hole wavefunction, r_e (r_h) is the electron (hole) coordinate, and Ω is the volume of the unit cell. The integral $\mathcal{F}_S(r)$ runs over all $|r|$ in Ω . In practice, it is computed for a set of 10 hole positions, on a dense grid (same one as the fine grid used in the BSE calculation), using a $20 \times 20 \times 1$ supercell for the TMD, a $10 \times 10 \times 1$ supercell for the molecular, and a $20 \times 10 \times 1$ supercell for the HBC. The projections of $\mathcal{F}_S(r)$ are shown in Fig. 3c. It is to be noted that the Bloch exciton is a periodic function in the center of mass coordinate $r = 1/2(r_e + r_h)$, and we have plotted just part of the wavefunction for a fixed r_h . We select the isosurface to include 98% of the electron density.

Estimation of misorientation angles

From the binary STM images, each molecule is treated as an ellipse with a centroid (x_c, y_c) . The centroids represent the geometric center of individual molecule, while the major axis depicts the long axis of the molecule. For a binary image, the centroid is defined as:

$$x_c = \frac{\sum x \cdot I(x, y)}{\sum I(x, y)}, \quad y_c = \frac{\sum y \cdot I(x, y)}{\sum I(x, y)}$$

Where $I(x, y)$ is the intensity of the binary image at pixel (x, y) , with $I(x, y) = 1$ for foreground pixels and $I(x, y) = 0$ for background pixels.

The orientation of individual molecule, relative to a horizontal reference axis, is derived using the second-order moments of the pixel distribution. These moments are calculated relative to the centroid of the ellipse (or molecule). The second-order central moments are calculated as:

$$M_{xx} = \sum (x - x_c)^2 \cdot I(x, y), \quad M_{yy} = \sum (y - y_c)^2 \cdot I(x, y), \quad M_{xy} = \sum (x - x_c)(y - y_c) \cdot I(x, y)$$

The orientation angle (\emptyset) is then computed as:

$$\emptyset = \frac{1}{2} \arctan \left(\frac{2M_{xy}}{M_{xx} - M_{yy}} \right)$$

Here, (x_c, y_c) represents the centroid, which serves as the reference point for calculating the relative coordinates $(x - x_c)$ and $(y - y_c)$ used in the moments.

The major axis length (α) is determined based on the pixel distribution along the principal axis of the ellipse. For visualization, the centroid (x_c, y_c) serves as the anchor point, and the major

axis is represented as a line segment. The endpoints (a, b in Supplementary Fig. 3) of the major axis for a single molecule are computed as:

$$a_i(x, y) = \left(x_c - \frac{\alpha}{2} \cos \phi, y_c - \frac{\alpha}{2} \sin \phi \right), \quad b_i(x, y) = \left(x_c + \frac{\alpha}{2} \cos \phi, y_c + \frac{\alpha}{2} \sin \phi \right)$$

Thus, we calculate the Cartesian coordinates for all molecules within the STM field of view. For PDI, the molecular orientation is measured with respect to the y-axis, taken as zero. For PTCDA and MePDI, the orientation of each molecule's major axis is determined relative to the major axes of its four nearest neighbors. These angular measurements are then used to generate histograms. The resulting histograms are fitted with normal distribution or probability density function (PDF) of the form:

$$f(x) = \frac{1}{\sigma\sqrt{2\pi}} e^{-\frac{(x-x_0)^2}{2\sigma^2}}$$

Where x_0 is the center of the distribution and σ is the standard deviation. For the PDI histogram, x_0 is equivalent to the molecular orientation, represented by the misorientation angle ξ . A value of ξ close to zero implies a highly aligned molecular lattice. For PTCDA and MePDI—where the molecules are significantly misaligned—the misorientation angle (ξ) is calculated as the difference between the x_0 values in the angular distribution, and the overall error in ξ is calculated as the root-sum-square (RSS) of individual standard deviations (σ).

Estimation of dipolar anisotropy from a vector model

We developed an empirical vector-trigonometric model to estimate the dipolar anisotropy within molecular lattices, specifically for PDI, MePDI, and PTCDA, in which the dipole moment (μ) is known to be oriented along the long axis of the single molecule. This model employs the trigonometric relationships between the μ vectors to estimate the relative dipolar anisotropy without considering intermolecular interactions. Instead, it focuses on providing an intuitive understanding of how the intrinsic geometric arrangement of molecules within these lattices may lead to differences in dipolar or optical anisotropy.

In our model, first, we fixed a reference unit vector ($\mu_1 = [1, 0, 0]$) representing a dipole moment aligned to X-axis. A second dipole moment vector ($\mu_2 = [\cos \xi, \sin \xi, 0]$) was then placed such that it makes an angle relative to μ_1 , where the direction of μ_2 changes with the misorientation angle (ξ) (Supplementary Fig. 18). Within a molecular lattice, the single molecular

dipole vectors were summed to produce lattice dipole vector (μ_+): $\mu_+ = \mu_1 + \mu_2 = [1 + \cos \xi, \sin \xi, 0]$, with its magnitude:

$$\|\mu_+\| = \sqrt{(1 + \cos \xi)^2 + \sin^2 \xi} = \sqrt{2(1 + \cos \xi)}$$

Similarly, subtraction leads to lattice dipole vector (μ_-): $\mu_- = \mu_1 - \mu_2 = [1 - \cos \xi, -\sin \xi, 0]$, with its magnitude:

$$\|\mu_-\| = \sqrt{(1 - \cos \xi)^2 + \sin^2 \xi} = \sqrt{2(1 - \cos \xi)}$$

Finally, we calculate dipolar anisotropy as:

$$\Delta\mu = \frac{1}{\sqrt{2}} (\|\mu_+\| - \|\mu_-\|)$$

Where the error in $\Delta\mu$ is calculated as: $\frac{1}{\sqrt{2}} |\cos(\xi + \sigma) - \cos(\xi - \sigma)|$

The pre-factor ensures that $\Delta\mu$ reaches a maximum value of 1 when the dipoles are fully aligned (i.e., $\xi = 0^\circ$), and a minimum value 0 when the dipoles are fully orthogonal (i.e., $\xi = 90^\circ$). This scaling aligns the model with expected physical limits of reflection anisotropy (RA), which are experimentally determined.

Method of PL data acquisition

Our PL measurements were conducted using a home-built optical setup integrated with LabView user interfaces. To ensure precise control over excitation power, we implemented a power control module, guaranteeing consistent excitation power throughout the measurements. For angle-dependent PL data acquisition with linearly polarized excitation, we adjusted the orientation of a half waveplate common to both the excitation and detection paths. To capture circularly polarized PL data, we reconfigured the polarizer setup to generate circularly polarized excitation, employing a quarter waveplate on the excitation side. A similar configuration was employed for acquiring wide-field PL images as reported in this study. On the detection side, we placed a premium-edge 550 nm long-pass filter between the beam splitter and the polarizer to eliminate residual excitation signals from the 532 nm excitation source. To select our desired emission wavelength, we incorporated two tunable filters as band-pass (Semrock; 550–620 nm with a 10 nm bandwidth) and directed the emitted beam through a condenser or tube lens to the detector. The optical setup is schematically depicted in Supplementary Fig. 8. The values of the full width half maxima for peaks **X**, **Y**, and **W** were extracted from first-order Gaussian fits to raw PL data. Additionally, to identify the origin of the sharp features in the PL spectrum, we used a 520 nm diode laser (linewidth greater than that of 532 nm) for excitation.

Calculation of optical anisotropy

Photoluminescence anisotropy: To calculate PL anisotropy (φ), we used the formula: $\varphi = \frac{I_{\max} - I_{\min}}{I_{\max} + I_{\min}}$, where I_{\max} and I_{\min} represent the maximum and minimum PL intensities recorded from a single crystalline HBC domain. These I_{\max} and I_{\min} values were extracted from the first-order Gaussian fits to the raw PL intensity vs. energy data for PL peaks labelled as **W**, **X**, and **Y** (see Fig. 2). We also calculated the extinction ratio as $\left(\frac{I_{\max}}{I_{\min}}\right)$ and the extinction (in dB) as $10\log_{10}\left(\frac{I_{\max}}{I_{\min}}\right)$. The extracted values for anisotropic PL peaks are as follows: for **X** ($E = 2.13$ eV), an extinction ratio of 57.06 and an extinction of 17.56 dB; and for peak **Y** ($E = 1.98$ eV), an extinction ratio of 10.59 and an extinction of 10.25 dB. The angle-dependent PL intensities were fitted using a cosine-squared function of the form: $I(\theta) = I_0[\cos(\theta - \theta_0)]^2$, where I_0 is the peak intensity and θ_0 is the phase offset.

Reflection contrast and anisotropy: For cross-polarized reflection measurements, the differential reflectance or reflection contrast ($\Delta R/R$) was calculated as $\Delta R/R(x, y, \lambda) = \frac{\{(R_{\text{HBC}} - R_{\text{dark}}) - (R_{\text{sub}} - R_{\text{dark}})\}}{R_{\text{sub}} - R_{\text{dark}}}$, where R_{HBC} , R_{sub} , and R_{dark} denote reflected intensities recorded from the HBC domain, the bare TMD substrate without the molecular monolayer, and the dark counts, respectively.

Reflection anisotropy (RA) values were extracted from the polarized reflectance spectra by using the formula: $2 \times \frac{R_{\parallel} - R_{\perp}}{R_{\parallel} + R_{\perp}}$, where R_{\parallel} and R_{\perp} are the reflected intensities recorded from a single crystalline HBC domain oriented parallel and perpendicular, respectively, relative to the direction of the incident linear polarization.

Calculation of the thermal activation energy of exciton

In order to extract the activation energy for the exciton corresponding to the PL peak **X** in Fig. 2g, we fitted the temperature-dependent PL intensities with a thermal dissociation (Arrhenius) equation: $I(T) = I(0)/[1 + \beta e^{-E_a/k_B T}]$, where $I(T)$, $I(0)$, β , k_B , and E_a are the PL intensity at temperature T , an initial intensity value (for $T = 0$), a pre-exponential factor, the Boltzmann constant, and the thermal activation energy of the exciton, respectively. We note that these PL intensity values did not require multiple energy scales or dissociation channels (e.g., E_{a1} , E_{a2} etc.) to fit versus T .

Analysis of crystalline domain structures

Our analysis of both single- and polycrystalline molecular domains on single crystal TMD involved the following procedure. For single crystal HBCs, we defined an arbitrary upright position for the triangular single-crystal domain, which is terminated with a zigzag edge, verified by the selected area electron diffraction (SAED in HRTEM; Supplementary Fig. 23). We then rotated the sample stage until achieving a maximum reflected intensity (brightest) from the domain. Data points were systematically acquired at multiple angles (θ_i) with small increments ($\sim 10^\circ$) around the angle corresponding to the maximum reflected intensity, as depicted in Supplementary Fig. 23. These reflected intensities were plotted against θ , and the angle associated with maximum intensity, denoted by θ_{max} , was determined via a cosine-squared fit to the raw data. This process was iterated for more than 50 randomly selected individual single-crystalline and polycrystalline PDI domains on single-crystal (triangular) WS_2 domains, generating the polar histograms shown in Fig. 4f.

Ionic gate spectroscopy

The ionically gated transistors²⁰ are composed of (1) Pt reference and counter electrodes to control the gate voltage (V_g); (2) Au contacts; and (3) HBC (PDI/ WS_2) channel. The electrodes were patterned with photolithography (Heidelberg MLA 150) and deposited by e-beam evaporation, and lift-off was carried out in acetone. The Au contacts were covered with e-beam deposited SiO_2 to avoid leakage current. The HBC channels were dry-transferred in vacuum,²¹ and patterned by photolithography. DEME TFSI (Sigma Aldrich) was used as ionic liquid. The device was encapsulated with PDMS and coverslip in an Ar-filled glove box with H_2O and O_2 levels less than 1 ppm. The V_g was applied and monitored by EC301 (Stanford Research Systems), and the current was measured with a preamplifier. The optical reflectance spectra were collected with a 40 \times objective (NA=0.6), dispersed by a spectrograph, and recorded by a CMOS camera. All transport measurements were synchronized with the optical measurements through LabView interface.

Calculation of lattice density and equivalent twist angle

To plot the lattice density vs. twist angle for a MoS_2/WS_2 bilayer superlattice (Fig. 4h), we first calculated the moiré period, $r(\theta)$, as follows:

$$r(\theta) \simeq \frac{a_{larger}}{\sqrt{\delta_a^2 + 4 \sin^2(\theta/2)}}; \delta_a = 1 - \frac{a_{larger}}{a_{smaller}}$$

Here, a_{larger} ($a_{smaller}$) is the larger (smaller) lattice constant among the two layers, δ_a is the lattice mismatch between the monolayer crystals, and θ is the interlayer twist angle. The area of the moiré unit cell, $A(\theta)$, was calculated as:

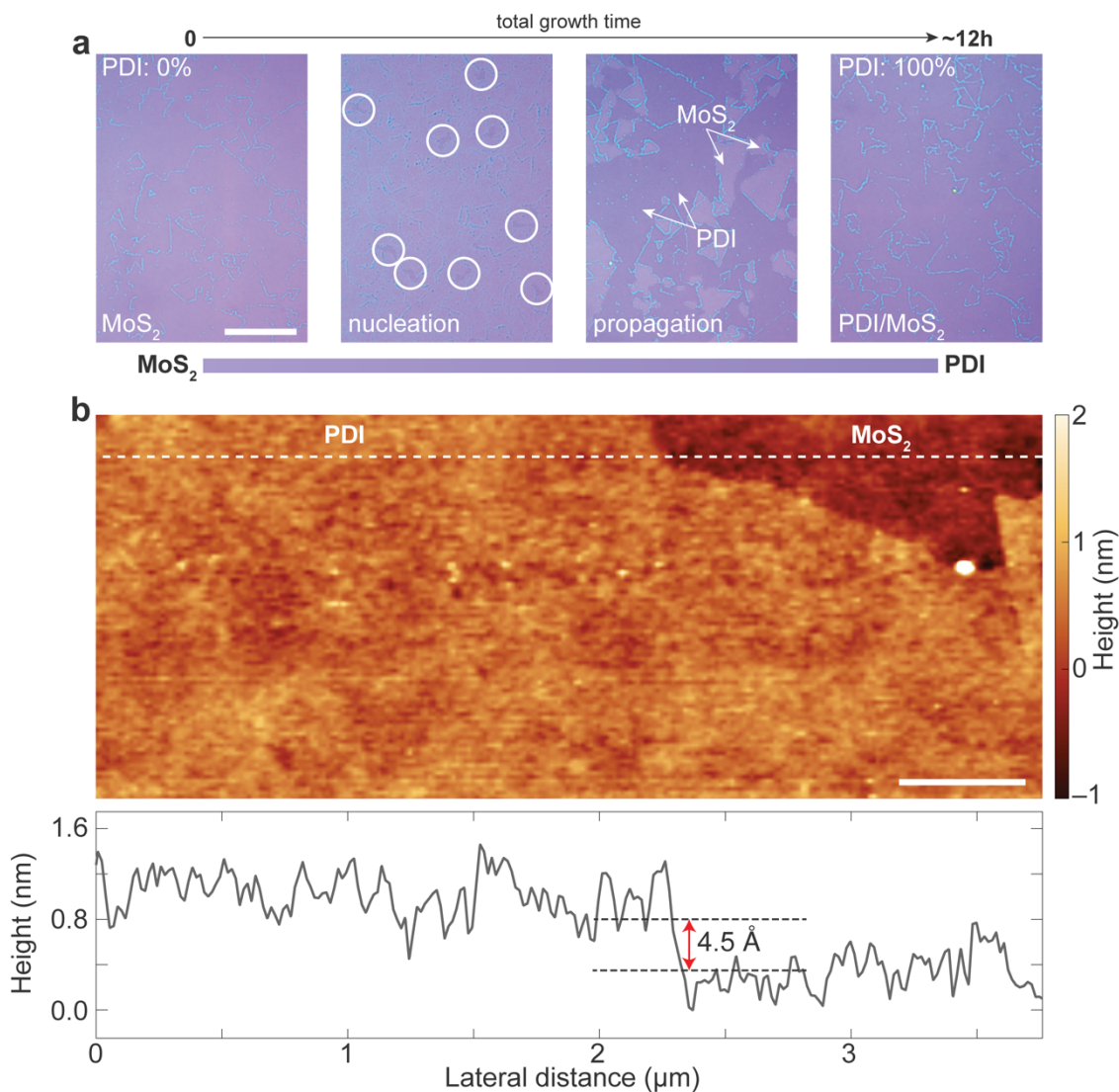
$$A(\theta) = (\sqrt{3}/2) \times r^2(\theta) \text{ in the unit of cm}^2$$

Next, the lattice density, $n(\theta)$, was expressed as $1/A(\theta)$ in the unit of cm^{-2} , and plotted against θ for the MoS_2/WS_2 bilayer.

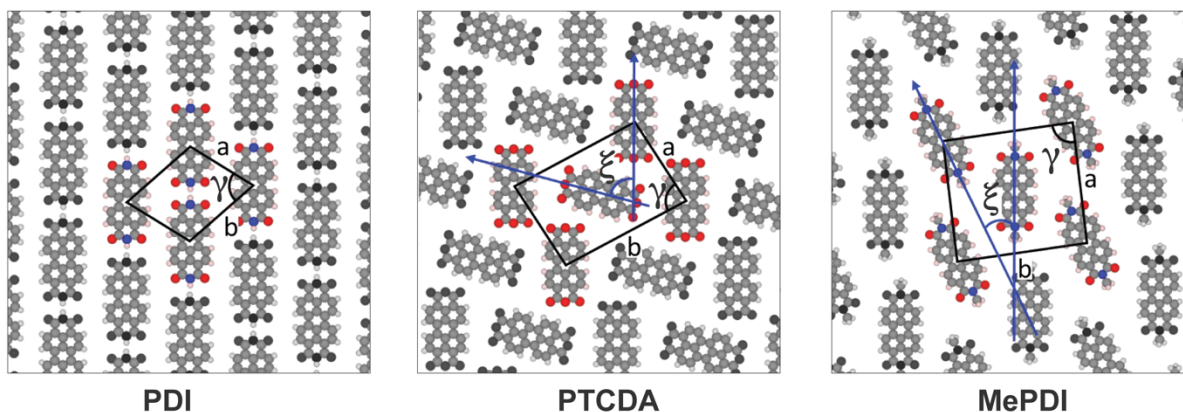
We then calculated the 2D molecular lattice densities for PDI, MePDI, and PTCDA from the parameters reported in Supplementary Table 1, extracted from the pixel-based analysis of the STM images. These values were then positioned on the y-axis, and parallel lines were extrapolated from these points to intersect the plot. The equivalent twist angle values were projected from the intersection points relative to the MoS_2/WS_2 bilayer. Additionally, two other molecular unit cell dimensions (sides of 30Å and 50Å; taken from literature) were included in the plot. The extracted values (relative to MoS_2/WS_2 bilayer) for the molecular crystals are given below:

Molecular Crystals	θ (°)	$n(\theta)$ (cm^{-2})	$r(\theta)$ (Å)
<i>PDI</i> (1)	16.3	9.0×10^{13}	11.3
<i>PTCDA</i> (3)	11.3	4.4×10^{13}	16.2
<i>MePDI</i> (2)	10.3	3.7×10^{13}	17.7
<i>Mol</i> – 1	5.7	1.1×10^{13}	32.2
<i>Mol</i> – 2	3.4	4.0×10^{12}	53.8

Supplementary Figures



Supplementary Fig. 1. Morphology and topography of HBC. (a) Optical images of monolayer PDI on monolayer MoS₂ surface at different stages (e.g., nucleation, propagation, and full coverage; left to right) of growth. Color bar denotes gradual and homogeneous change in contrast from MoS₂ (lighter) to PDI (darker) regions. Scale bar: 20 μm. (b) AFM height map of PDI/MoS₂ consisting of partially grown PDI molecular crystal grown on top of MoS₂ monolayer (top). AFM height profile taken along the dashed white line in the height map (bottom). Scale bar: 500 nm.

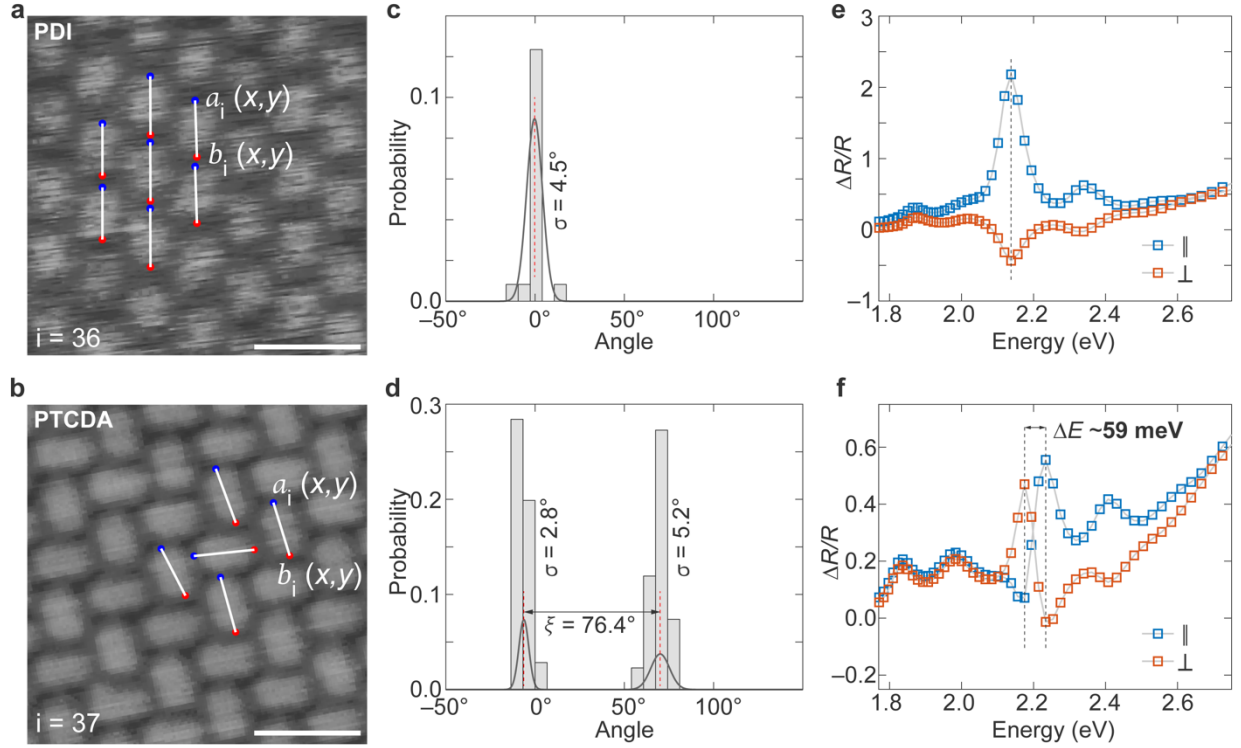


PDI

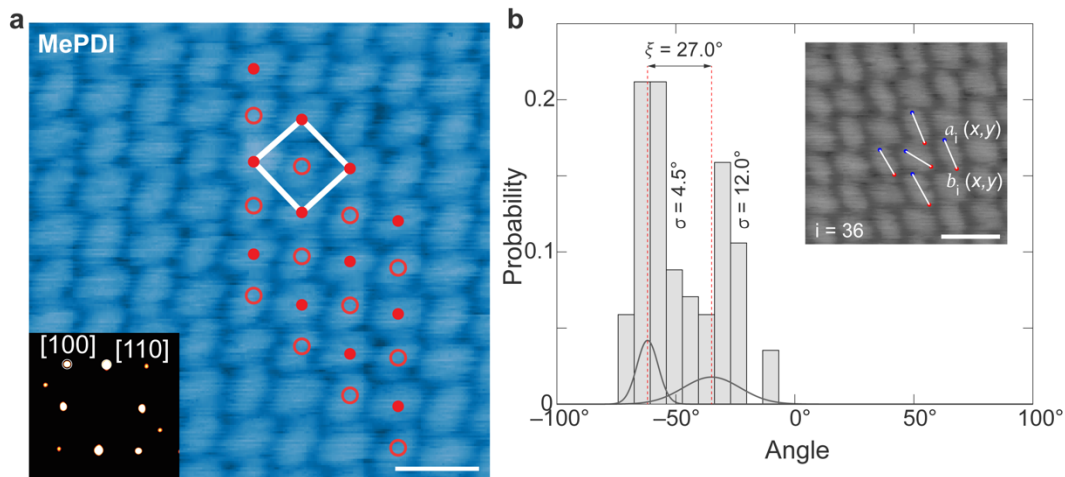
PTCDA

MePDI

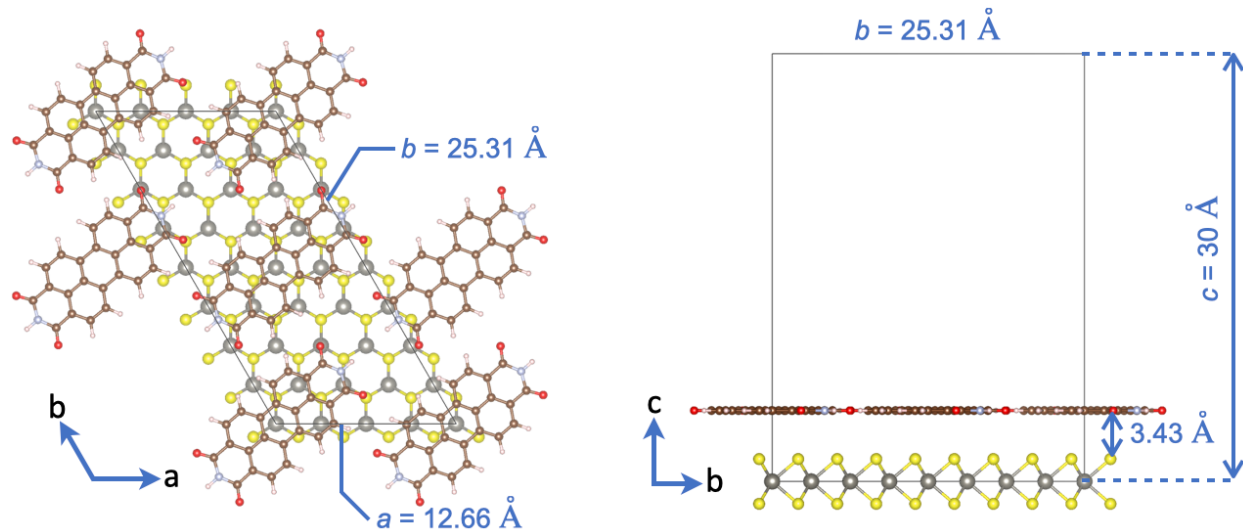
Supplementary Fig. 2. Molecular lattice structures. Schematic top-view (not to scale) of molecular lattices consisting of PDI, PTCDA, and MePDI molecules shown along with their corresponding unit cells (black boxed regions). STM-derived lattice parameters (a , b , γ , ξ) are given in Supplementary Table 1.



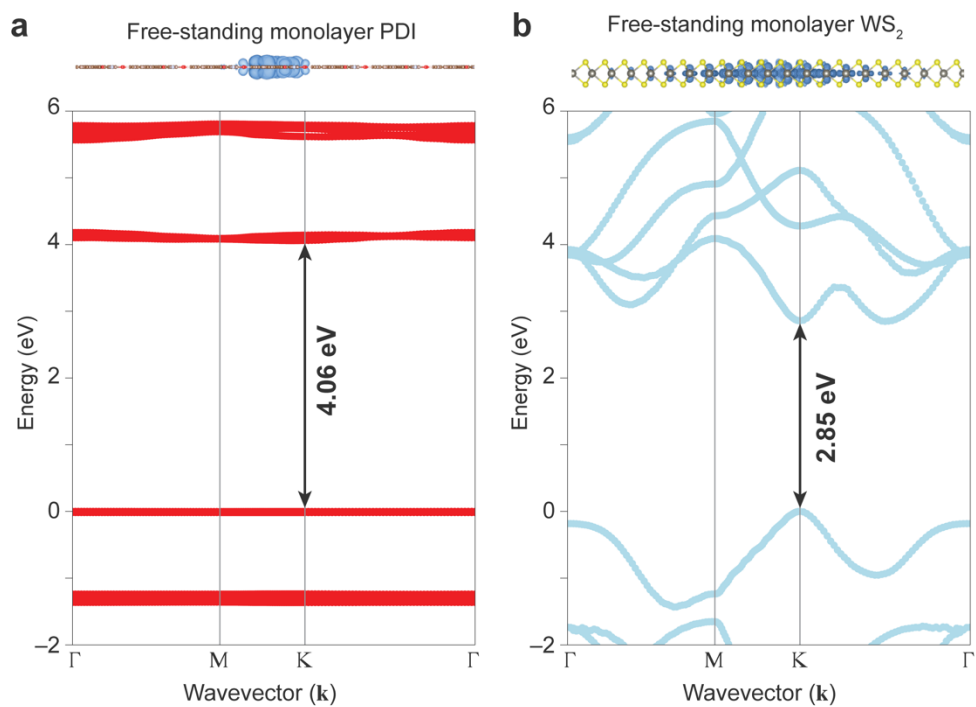
Supplementary Fig. 3. Estimation of misorientation angles (ξ). Binary cropped-STM images of monolayers of (a) PDI and (b) PTCDA on monolayer MoS₂. Scale bar: 2 nm. Red and blue circles indicate molecular coordinates, and white lines indicate the major or long axis of the single molecule. Histograms depict the angular distribution between neighboring molecules. Misorientation angles (ξ) and standard deviations (σ) are extracted from first-order Gaussian fits or PDFs (grey lines) for (c) PDI and (d) PTCDA lattices. Red dashed lines highlight the center of each PDF. Room-temperature differential reflectance ($\Delta R/R$) spectra for molecular domains oriented parallel and perpendicular to the linear polarization are shown for (e) PDI and (f) PTCDA. Dashed lines mark characteristic excitonic signals.



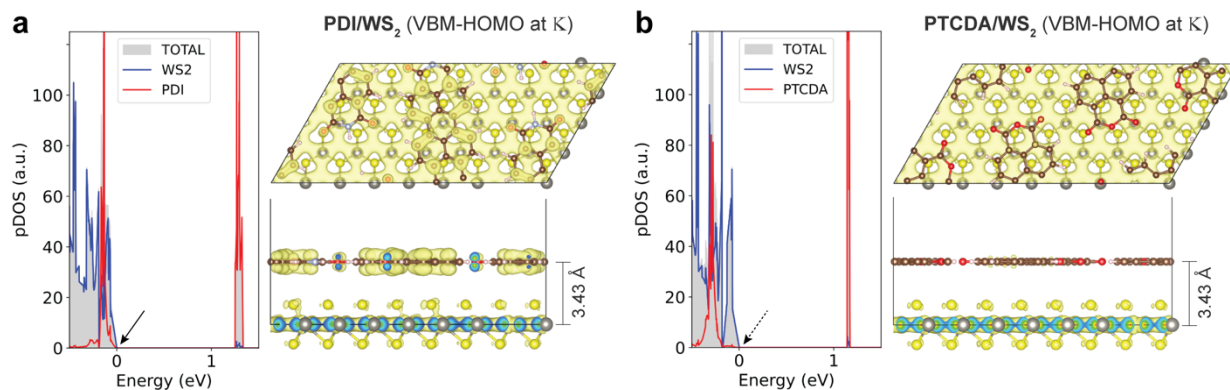
Supplementary Fig. 4. STM characterization of MePDI lattice. (a) Room-temperature STM image of MePDI grown on a MoS₂ monolayer. Solid and open red dots denote molecular lattice points. The white box outlines the molecular unit cell. *Inset*: Corresponding FFT image. Scale bar: 2 nm. (b) Histograms depicting the angular distribution between neighboring molecules. Red dashed lines highlight the center of each PDF. Misorientation angles (ξ) and standard deviations (σ) are extracted from the PDFs (grey lines). *Inset*: Binary cropped-STM image used to generate the histogram. Scale bar: 2 nm.



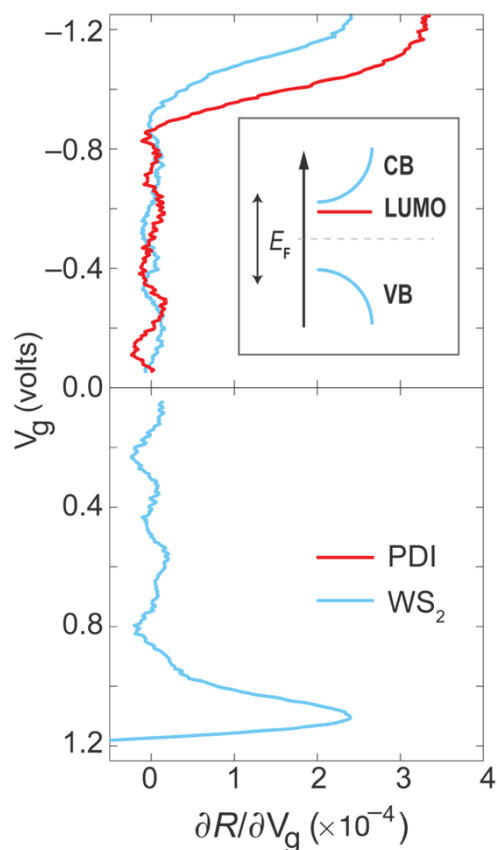
Supplementary Fig. 5. Computed PDI/WS₂ supercell. GW-computed supercell for PDI/WS₂ highlighting the lattice parameters used in our ab initio calculations. For the PDI monolayer, the primitive unit cell involves one PDI molecule. However, the supercell used for constructing the interface contains two PDI molecules. We use two molecules per unit cell because the supercell is built such that it can accommodate both the WS₂ parameters and the PDI parameters without having to stretch/compress too much any of the two layers. The optimal dimension of the supercell is obtained for a 4×8×1 supercell built on the WS₂ unit cell.



Supplementary Fig. 6. Computed band structures of freestanding monolayers. GW-computed quasiparticle band structures of monolayers of **(a)** PDI and **(b)** WS₂ crystals. Freestanding direct bandgap and HOMO-LUMO energies are highlighted with double sided arrows.

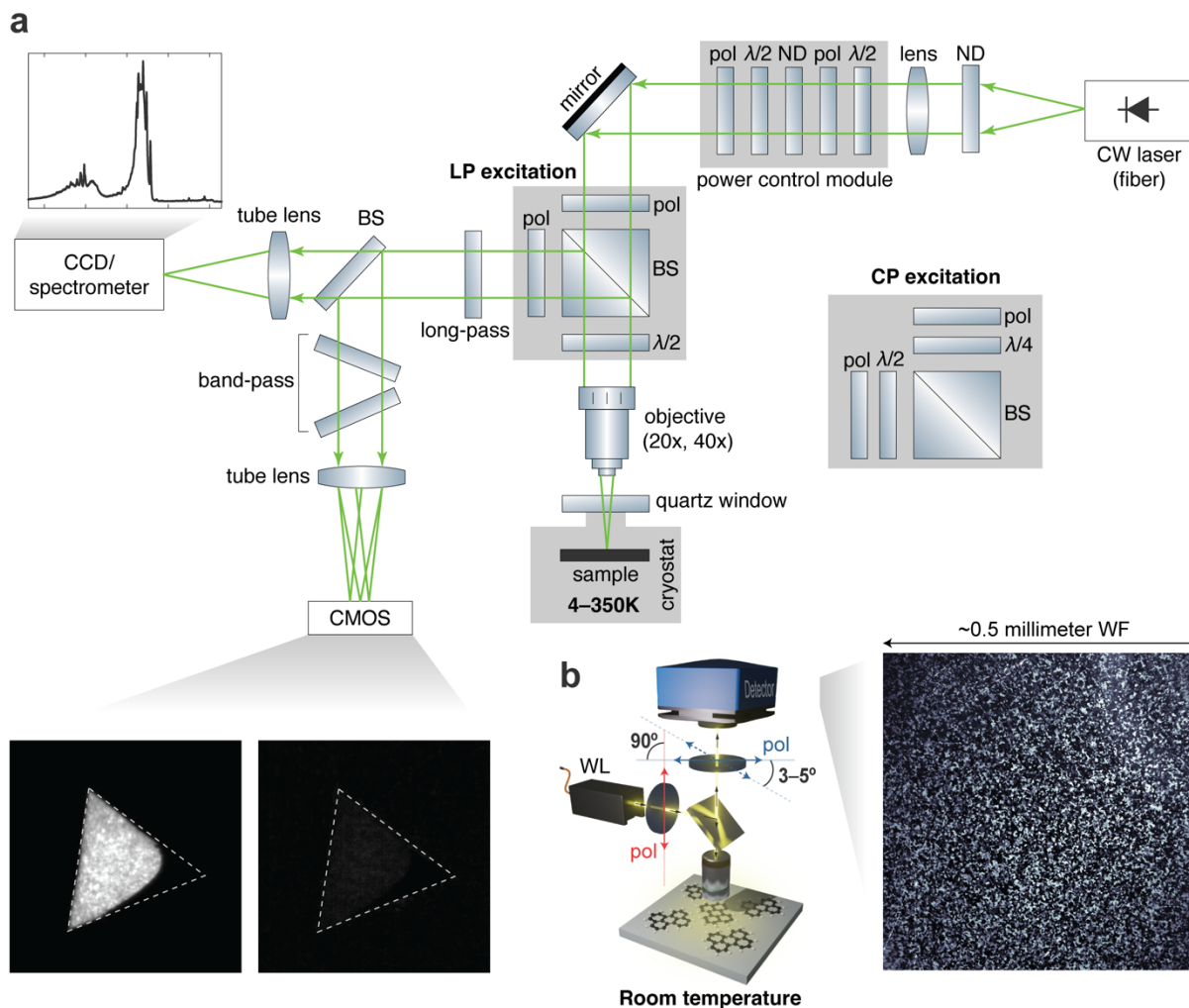


Supplementary Fig. 7. Computed density of states and square of wavefunctions at K point. DFT-calculated total density of states (grey) and projected density of states (pDOS; left), along with the square of the real-space VBM-HOMO wavefunctions (top and side views; right) at the high-symmetry K point for PDI/WS₂ (a) and PTCDA/WS₂ (b), each with an interlayer distance of 3.43 Å. Electron densities associated with *W-d*, *C-p*, and *O-p* orbitals are highlighted in yellow. Solid and dashed arrows highlight the pDOS at the band edges.



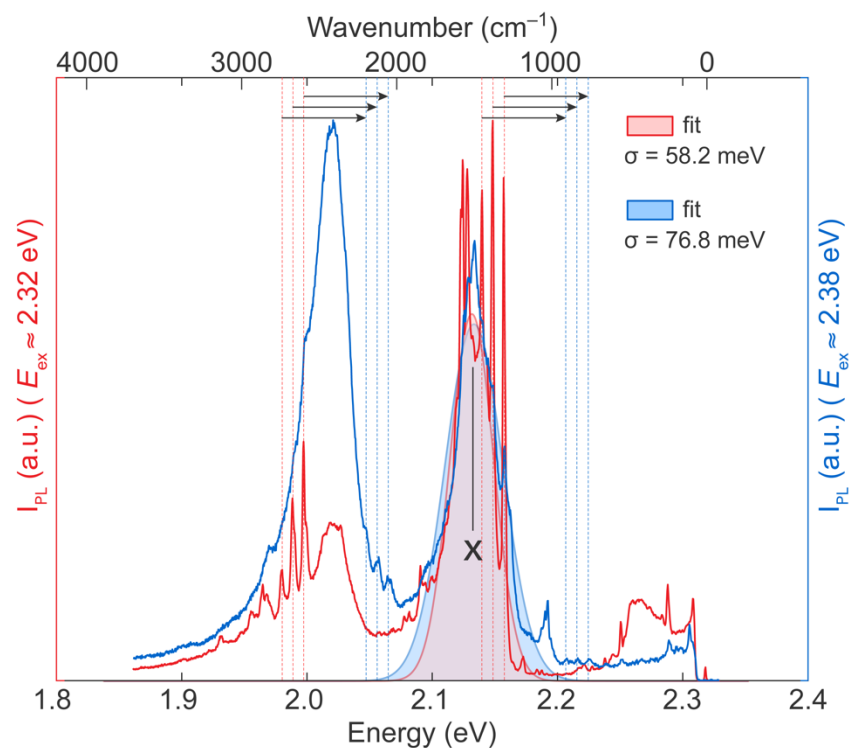
Supplementary Fig. 8. Electrochemical transport properties of PDI/WS₂. Plot of reflection (R) gradient with respect to gate voltage ($\partial R/\partial V_g$) versus V_g , showing the electron- and hole-doped regions corresponding to the spectral windows for PDI (red line; 2.2–2.3 eV) and WS₂ (blue line; 2.0–2.1 eV). *Inset:* Schematic of the energy level diagram showing the PDI LUMO level residing within the WS₂ band gap (E_F : Fermi energy).

Note: In the electron-doped region, the PDI level (LUMO) is reached prior to the WS₂ conduction band (CB) onset with a small energy difference between the molecular level and the conduction band edge. In the hole-doped region, however, the WS₂ valence band (VB) edge is reached first. This picture is consistent with our GW calculations (Fig. 1e and Fig. 3a). Under this measurement condition, the HOMO level of PDI could not be accessed due to possible molecular oxidation ($\text{PDI}^0 = \text{PDI}^{n+} + n\text{e}^-$) under large positive bias.

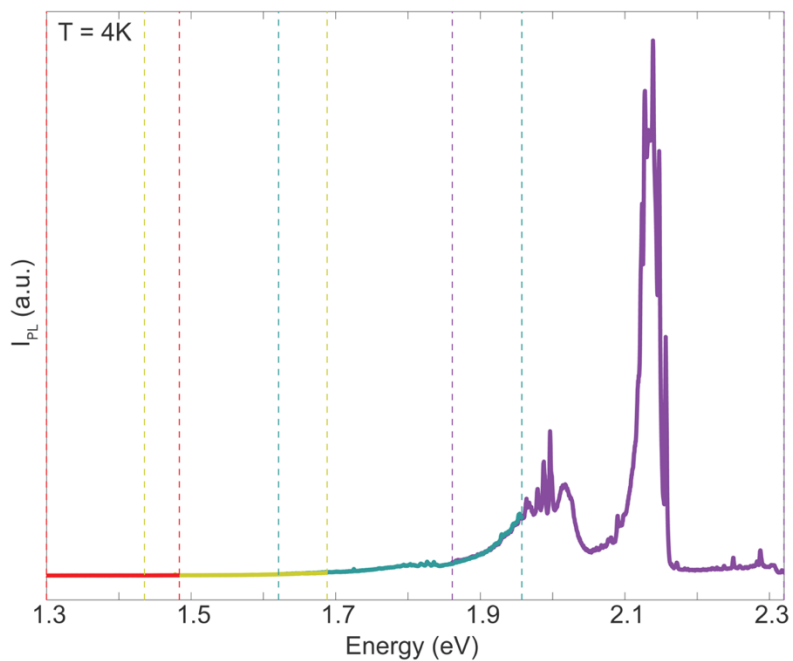


Supplementary Fig. 9. Home-built optical measurement systems. (a) Diagram (not to scale) of our home-built cryo-PL wide-field imaging and confocal spectroscopy system. **(b)** Schematic of our home-built cross-polarized (analyzer rotated about 3–5°) differential reflectance ($\Delta R/R$) hyperspectral microscopy set up.

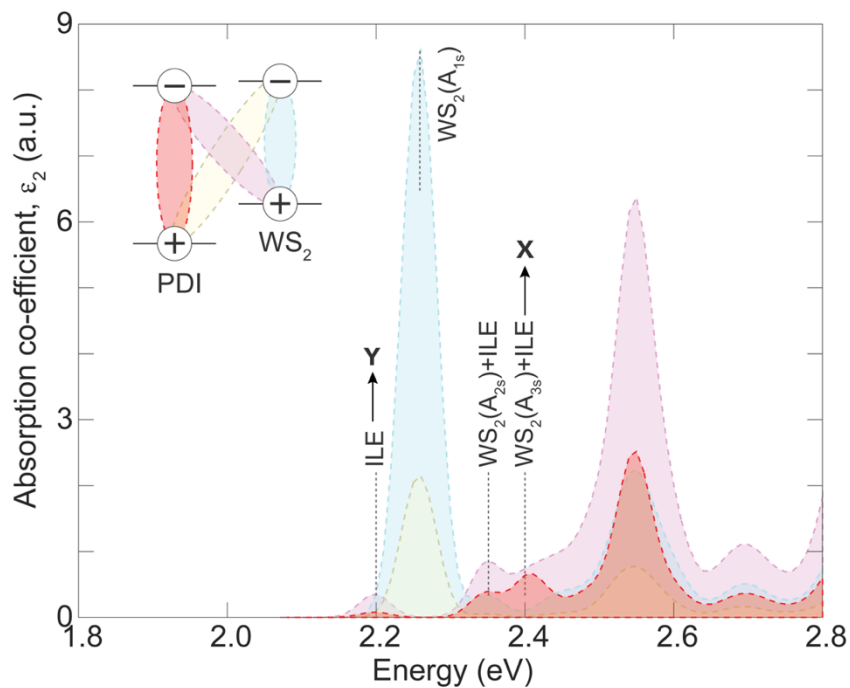
[CW: continuous wave; WL: white light; WF: wide-field; pol: polarizer; ND: neutral density filter; half-wave plate: $\lambda/2$; quarter-wave plate: $\lambda/4$; LP: linearly polarized; CP: circularly polarized; BS: beam splitter]



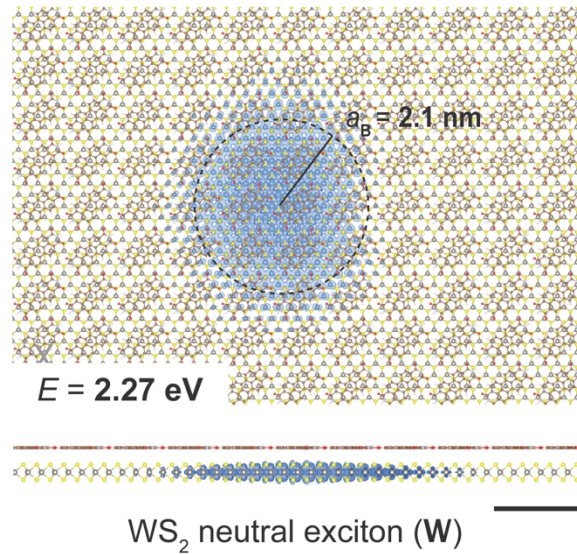
Supplementary Fig. 10. Identification of Raman modes of PDI/WS₂. PL spectra from a single-crystal PDI/WS₂ domain using two excitation sources: 2.32 eV (red) and 2.38 eV (blue) at T = 4 K. Both spectra show a prominent PL peak (X; solid line) centered at 2.13 eV, each overlaid with first-order Gaussian fits. The bandwidth (σ) values are shown in the inset. Copies of main aromatic Raman features are indicated by dotted red and blue lines.



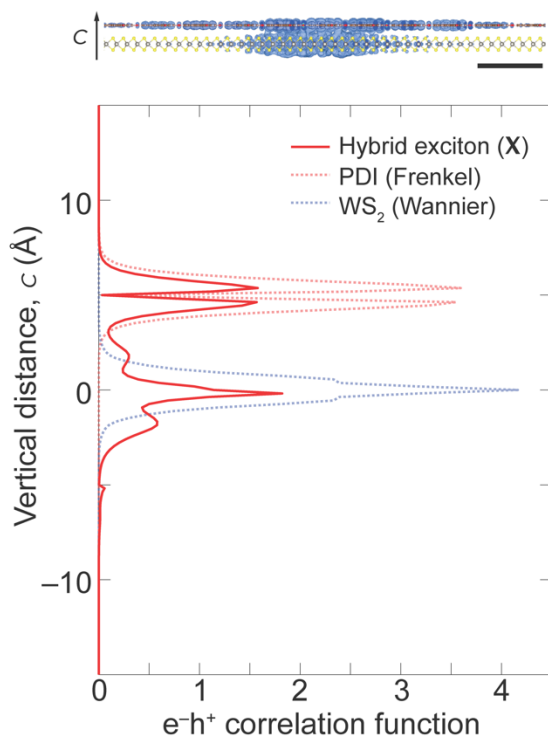
Supplementary Fig. 11. Wide-range PL spectra of PDI/WS₂. PL spectra collected from a single-crystal PDI/WS₂ domain measured at T = 4K, with different detection energy ranges highlighted by colored dotted lines.



Supplementary Fig. 12. Computed full absorption spectrum of PDI/WS₂. GW-BSE-computed imaginary components of the dielectric function (ϵ_2)—equivalent to the linear absorption spectrum—for PDI/WS₂ is plotted as a function of photon energy, showing the contributions from four distinct excitonic species: PDI intralayer (red), WS₂ intralayer (light-blue), low-energy interlayer exciton (ILE; pink), and high-energy ILE (yellow). *Inset:* Schematic of the type-II interface in PDI/WS₂ highlighting four excitonic transitions. The hybrid excitons are formed due to the overlap between low-energy ILE and the higher order Rydberg series (A_{2s} , A_{3s}) of WS₂.

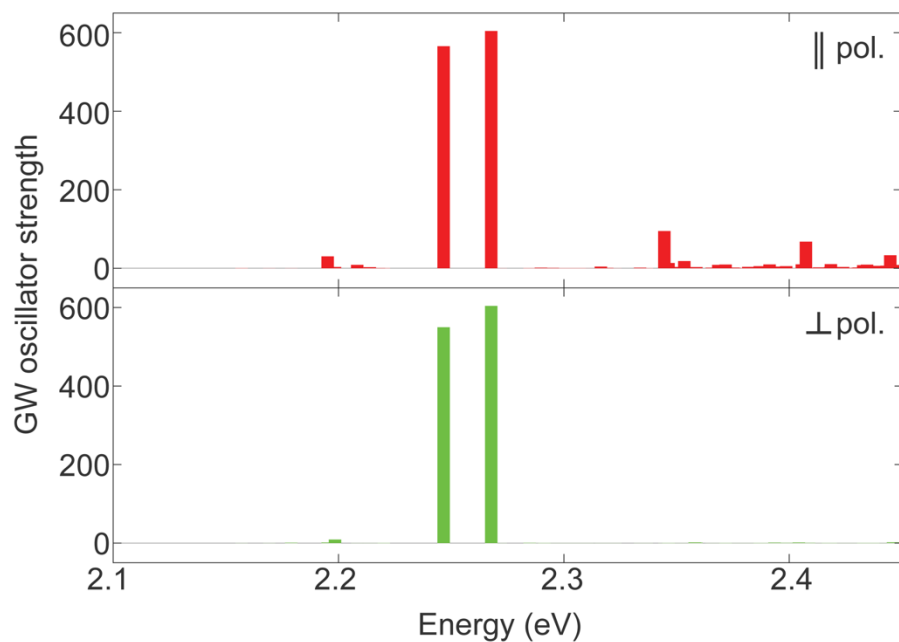


Supplementary Fig. 13. Computed electron isosurface map of WS₂ exciton. GW-BSE-calculated electron isosurface map of the WS₂ Mott-Wannier excitonic wavefunction (**W**) within PDI/WS₂. Scale bar: 2 nm.



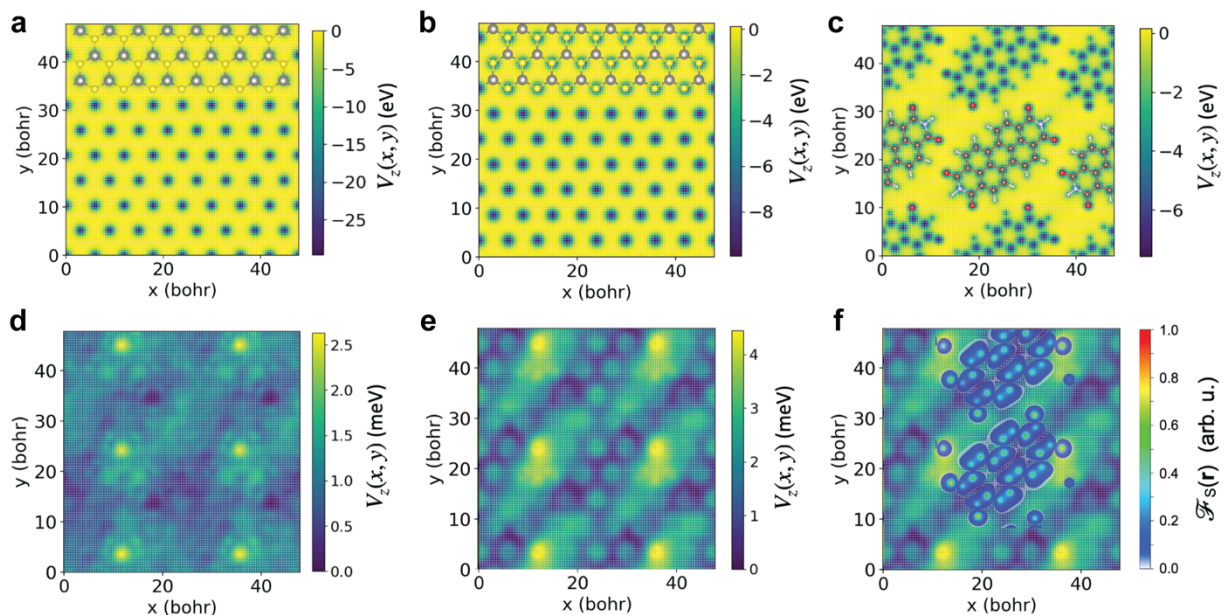
Supplementary Fig. 14. Computed vertical delocalization of hybrid exciton. GW-BSE-calculated electron-hole (e^-h^+) correlation function or wavefunction plotted against the crystallographic c direction (top) in PDI/WS₂, highlighting the hybrid exciton, **X** (red). The plots of e^-h^+ correlation functions for freestanding PDI (Frenkel; dotted red) and WS₂ (Wannier; dotted blue) excitons are shown together for comparison. Scale bar: 2 nm.

Note: The e^-h^+ correlation function of the hybrid exciton (**X**) extends across the two layers, with a lower probability in the vacuum between the layers.

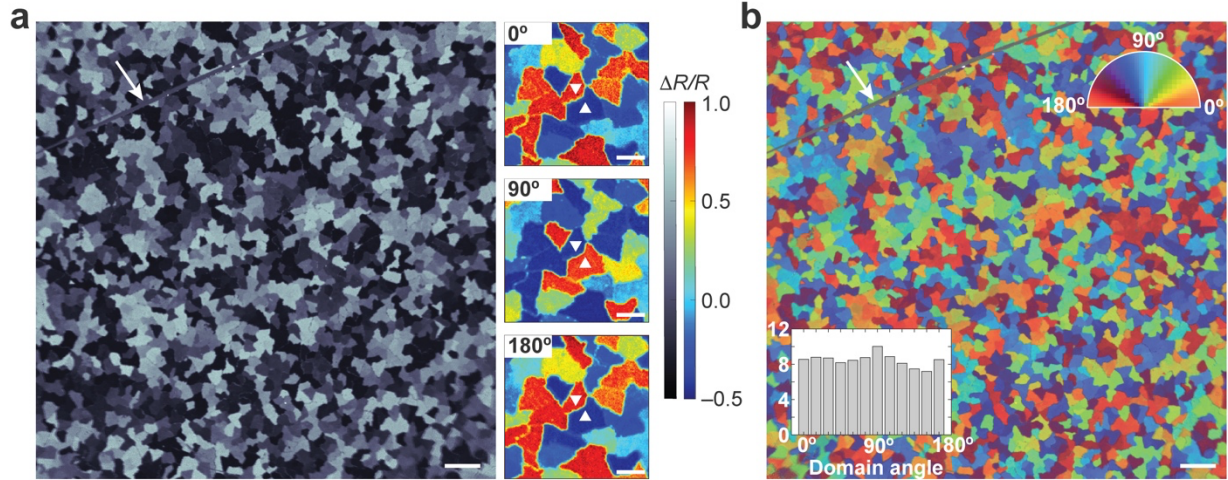


Supplementary Fig. 15. Computed oscillator strengths of excitons in PDI/WS₂. GW-computed oscillator strengths of excitons in PDI/WS₂ under parallel (red) and perpendicular (green) optical polarizations plotted against photon energies.

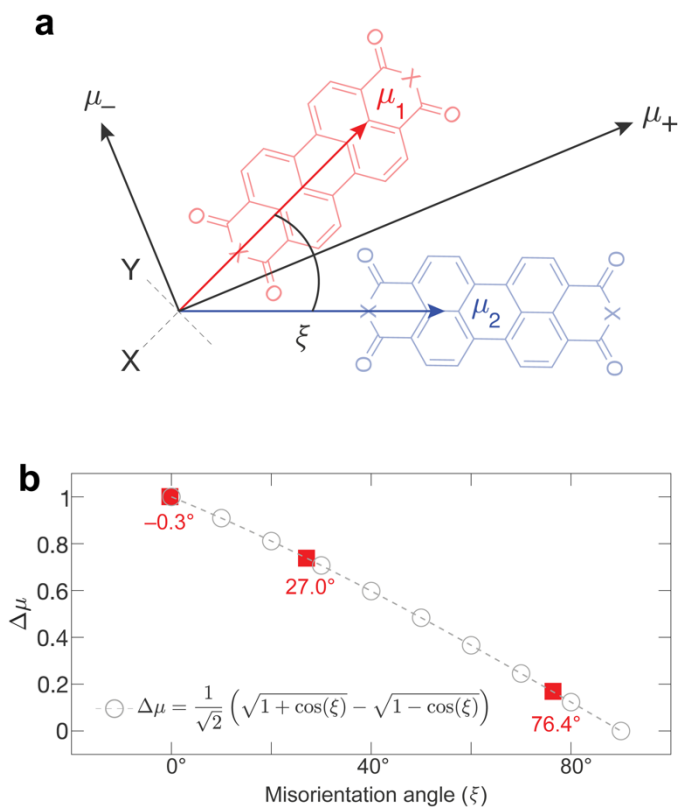
Note: In our exciton decomposition scheme, the excitons above 2.3 eV are of hybrid character with varying contributions from the molecular transitions.



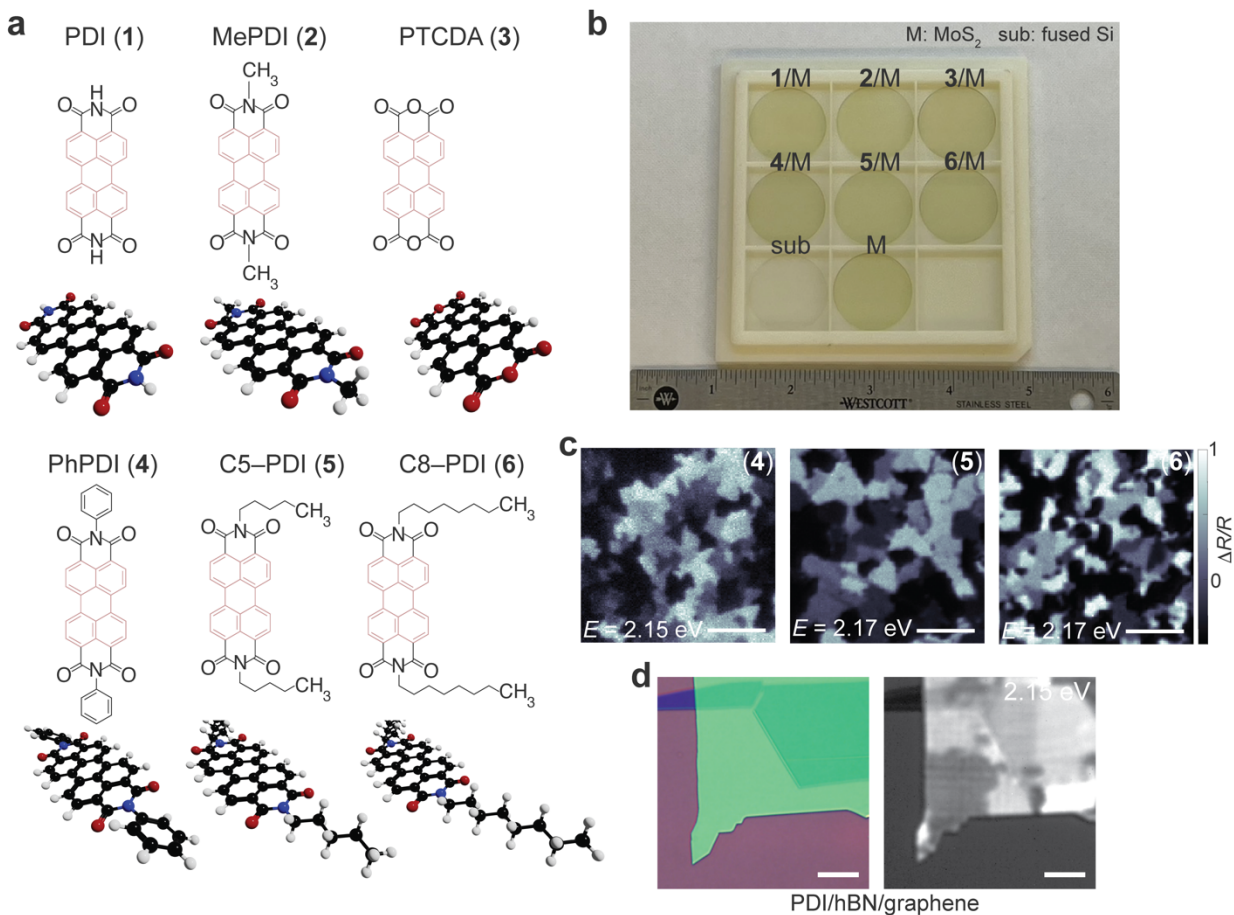
Supplementary Fig. 16. Computed potential well depths in PDI/WS₂. DFT potential (bare + Hartree), $V(x, y, z)$, computed for the PDI/WS₂ interface, shown for z (in reduced coordinates) at (a) 0, corresponding to the W atomic layer, (b) 0.12, corresponding to the top S atomic layer, and (c) 0.39, corresponding to the PDI molecular layer. The potential difference between the interface and the isolated WS₂ layer is shown at (d) $z = 0$, (e) $z = 0.12$, and (f) $z = 0.12$, with part of the electronic isosurface superimposed on the potential difference in (f). Spatial dimensions are in Å.



Supplementary Fig. 17. Poly-crystalline HBC domain structure analysis. (a) Room-temperature cross-polarized $\Delta R/R$ image (at 2.19 eV) of PTCDA/MoS₂ (left). Zoomed-in $\Delta R/R$ images (at 0°, 90°, and 180°) marking two mutually orthogonal laterally stitched single crystal domains by upright and inverted triangles (right). Scale bars: 20 μm . (b) False-colored image constructed by superposing three $\Delta R/R$ images at 0°, 45°, and 90° of the exact same field-of-view shown in (a; white arrows highlight a scratch on the sample). *Inset:* A histogram generated from the false color map showing a uniform angular distribution of individual single-crystal domains. Scale bar: 20 μm .

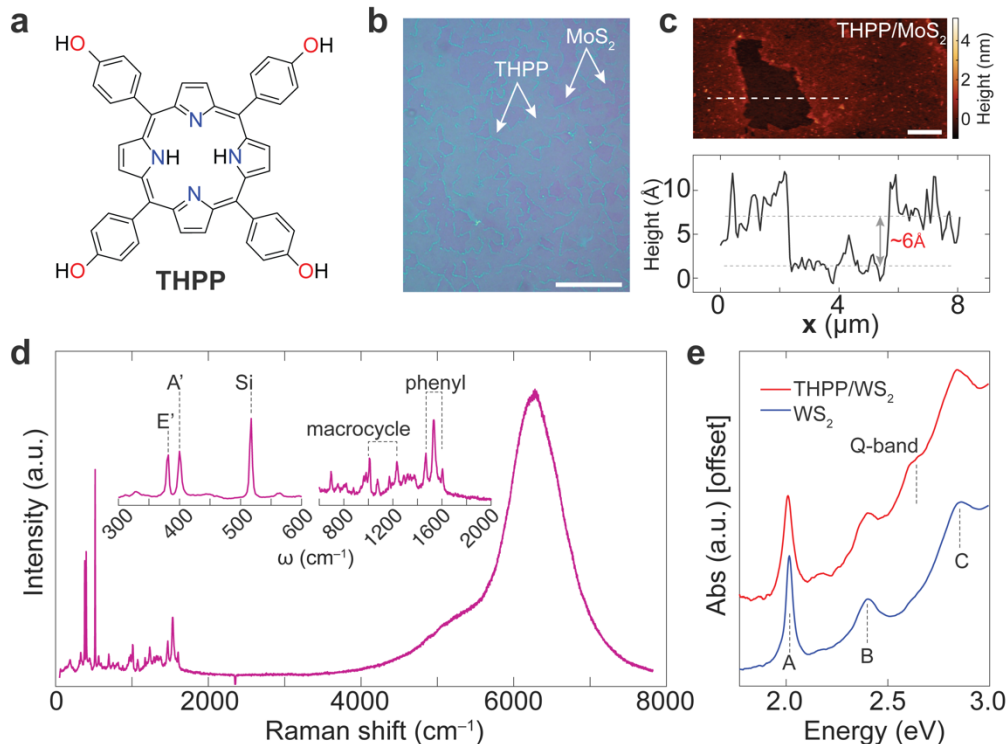


Supplementary Fig. 18. Vector model for dipolar anisotropy ($\Delta\mu$). (a) Vector diagram illustrating the arrangement of single-molecule unit dipoles (μ_1 and μ_2), decomposed into lattice dipole components (μ_+ and μ_-) on a 2D Cartesian plane, where the molecular dipoles form an angle ζ . (b) Plot of $\Delta\mu$ vs. ζ with their trigonometric relationship shown in the legend. Measured ζ values (red square markers) from the STM analysis are shown along with the model (grey circles and dashed line) for comparison.

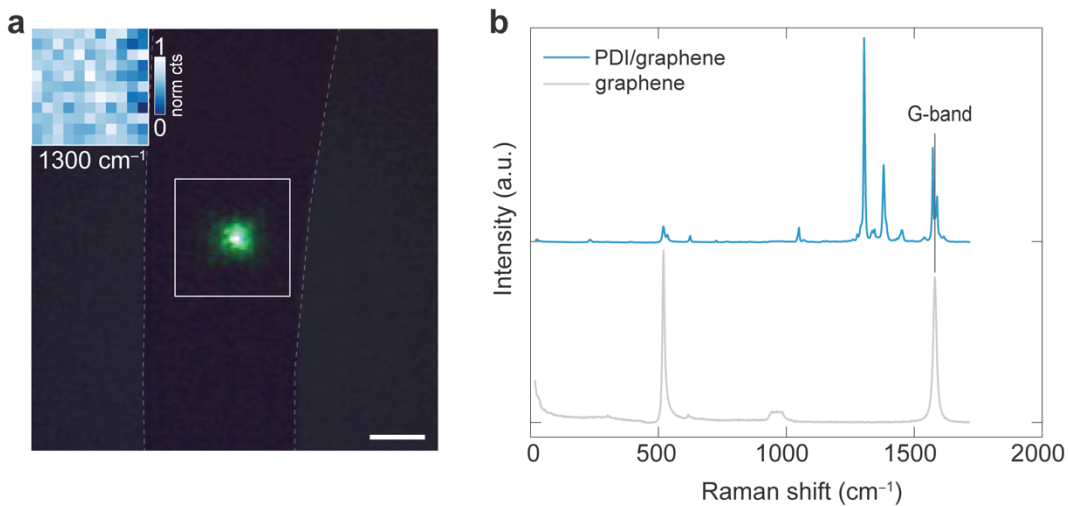


Supplementary Fig. 19. Wafer-scale synthesis and characterization of perylene-based HBCs.

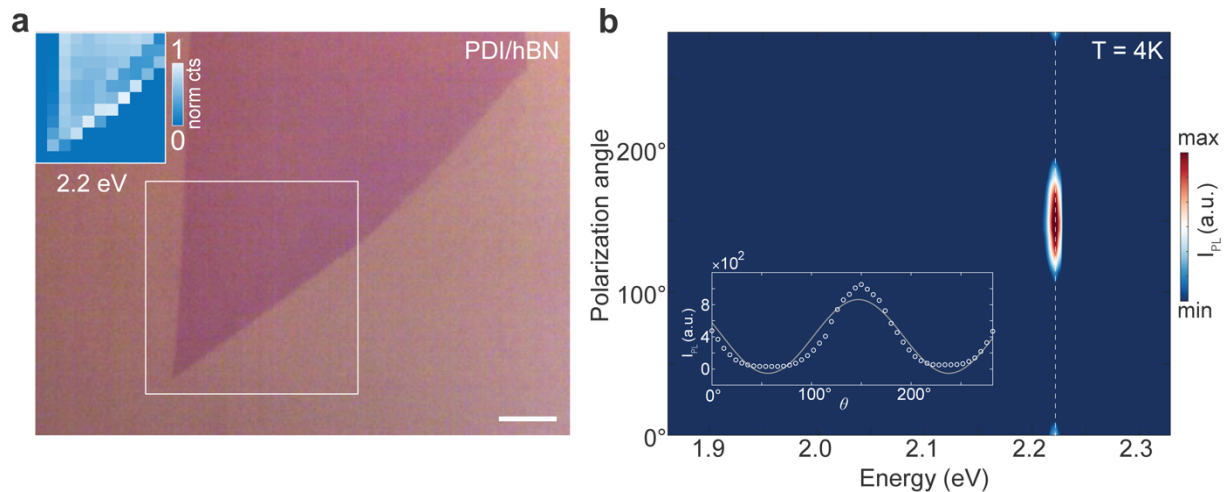
(a) The chemical structures and ball-and-stick models of the precursor molecules (1–6) used to synthesize the six different HBCs. (b) Wafer-scale continuous films of six different HBCs (e.g., 1/M) grown on 1 inch fused silica substrates shown along with a blank substrate (sub) and as-grown MoS₂ (M). (c) Cross-polarized $\Delta R/R$ images of as-grown PhPDI (4), C5-PDI (5), and C8-PDI (6) on polycrystalline MoS₂ monolayers. Scale bars: 20 μm . (d) Optical (left) and $\Delta R/R$ (right) images of PDI domains grown on exfoliated hBN on a graphene back-gate device. Scale bars: 10 μm .



Supplementary Fig. 20. Synthesis and characterization of porphyrin-based HBCs. (a) Chemical structure of the THPP molecule. (b) Optical image of a partially grown THPP/ MoS₂, showing contrast between the THPP and MoS₂ regions, indicated by arrows. Scale bar: 20 μm . (c) AFM height map of the THPP/MoS₂, showing a partially grown THPP molecular crystal on a MoS₂ monolayer (top). An AFM height profile taken along the dashed white line in the height map (bottom), with dashed lines serving as a guide for a $\sim 6\text{\AA}$ step height. Scale bar: 2 μm . (d) Raman scattering spectrum of the THPP/MoS₂, highlighting characteristic peaks for THPP (porphyrin macrocycle and phenyl C=C) and MoS₂ (dashed lines in the inset). (e) Room-temperature UV-vis absorption spectra of THPP/WS₂ along with that of monolayer WS₂, both samples transferred onto transparent fused silica substrates. Dashed lines indicate the signature of the porphyrin Q-band ($\sim 2.65\text{ eV}$)²² and A, B, C excitonic features of WS₂.

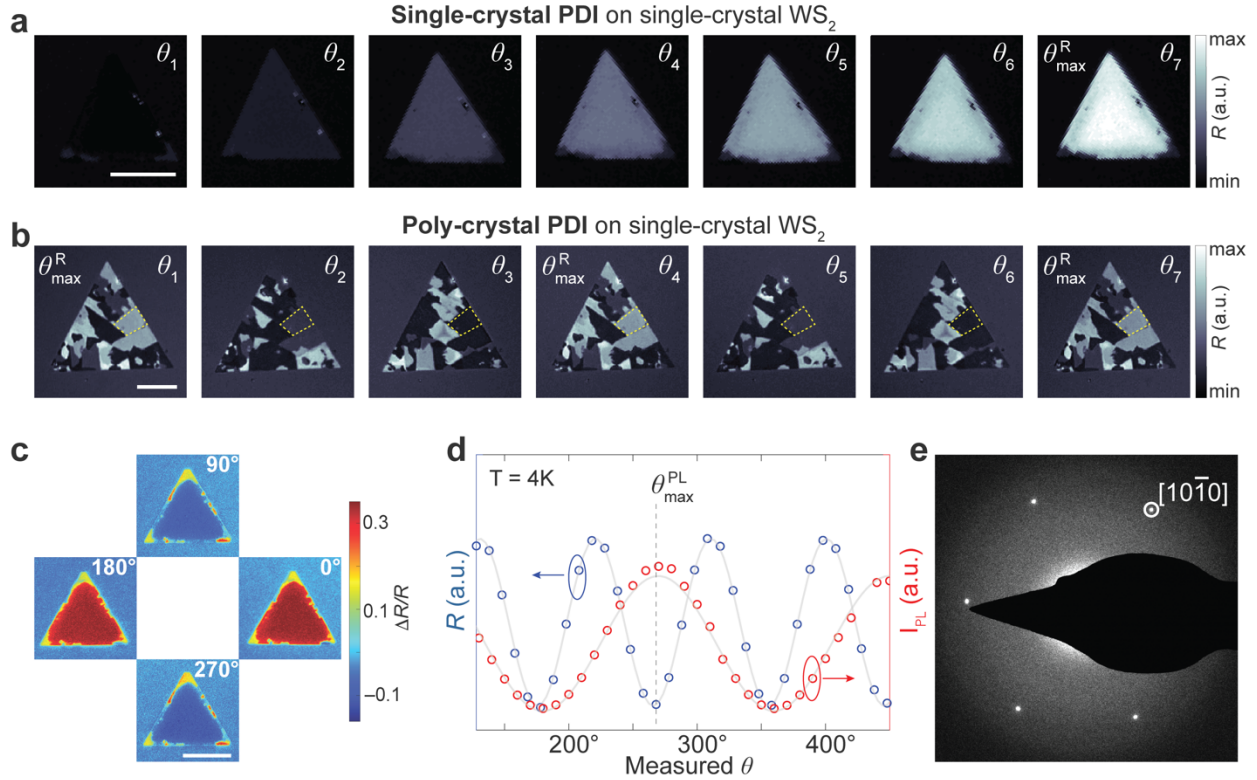


Supplementary Fig. 21. Synthesis and characterization of PDI/graphene. (a) Optical image of PDI grown on mechanically exfoliated graphene flake outlined by dotted white lines. *Inset*: Pixel-by-pixel Raman map (at 1300 cm^{-1}) collected from the white boxed region in the optical image using 532 nm excitation. Scale bar: $10\text{ }\mu\text{m}$. (b) Raman line spectrum of PDI/graphene (blue) shown along with that of graphene only (grey), highlighting graphene's G-band. While the characteristic aromatic Raman active modes are clearly visible between $1000\text{--}1500\text{ cm}^{-1}$ in PDI/graphene, the PL from PDI (see Supplementary Fig.8) is completely quenched on graphene.



Supplementary Fig. 22. Synthesis and characterization of PDI/hBN. (a) Optical image of PDI grown on mechanically exfoliated hBN flake. *Inset*: Pixel-by-pixel PL map (at $E \sim 2.2$ eV) collected from the white boxed region in the optical image using 532 nm excitation. Scale bar: 5 μm . (b) Polarization angle (θ)-dependent PL map collected from a PDI/hBN flake at $T = 4\text{K}$. A polarized PL signal is observed at $E = 2.22$ eV, highlighted by a dashed white line. *Inset*: θ vs. I_{PL} linecut along the dashed white line, overlaid with cosine-squared fit (gray).

Note: From the fitted data (inset; b), we calculate the PL anisotropy, extinction ratio, and extinction for PDI/hBN to be 0.96 (cf. 0.97 for **X**), 46.87 (cf. 57.06 for **X**), and 16.71 dB (17.56 dB for **X**), respectively.



Supplementary Fig. 23. Single- and poly-crystal PDI domains on single-crystal WS₂. Angle-dependent reflectance (R) images ($E = 2.15$ eV) of PDI single-crystals (a) and poly-crystals (b) on WS₂ single-crystal substrates at room temperature. θ_{\max}^R values from 53 single-crystal and 66 polycrystalline PDI domains (single-domain highlighted with dotted yellow line) were used to generate the polar histograms in Fig. 4f. (c) Cross-polarized $\Delta R/R$ images of a single-crystal PDI domain on WS₂ at four θ positions (90° apart), showing two-fold symmetry. Scale bar: $20 \mu\text{m}$. (d) Angle-dependent reflectance (blue) and PL intensity (red) from a PDI/WS₂ domain at $T = 4$ K, overlaid with cosine-squared fits (grey). Dashed line marks the angle $\theta_{\max}^{\text{PL}}$ corresponding to maximum PL intensity. (e) Selected area electron diffraction (SAED) in high-resolution TEM mode from a PDI/WS₂ domain, showing FFT peaks for TMD zigzag-terminated edges²³.

Supplementary Tables

	PDI	MePDI	PTCDA	MoS ₂ /WS ₂ ²⁴
$x_{0,1}$ (°)	-0.3	-34.9	-6.3	-
$x_{0,2}$ (°)	-	-61.9	70.1	-
$\xi = \Delta x_0$ (°) ^(a)	-0.3	27.0	76.4	-
σ_1 (°)	4.5	4.5	2.8	-
σ_2 (°)	-	12.0	5.2	-
$\sigma_{RSS} = \sqrt{\sigma_1^2 + \sigma_2^2}$ (°) ^(b)	4.5	12.8	5.9	-
a (Å)	9.1	15.7	11.6	3.1
b (Å)	10.6	16.7	17.2	3.1
γ (°)	69.5	85.8	85.8	120
Area (Å ²) = $ab \sin \gamma$	90.0	262.0	199.4	-
Basis	1	2	2	-

(a) ξ is calculated as the center-to-center distance (Δx_0) of the PDF in Supplementary Fig. 3 and 4.

(b) σ_{RSS} is calculated as the root-sum-square of the individual standard deviations in Supplementary Fig. 3 and 4.

Supplementary Table 1. Experimental lattice parameters. Molecular lattice parameters and misorientation angles obtained from the analysis of STM topography images. The TMD lattice parameters are shown alongside.

	WS ₂ unit cell	PDI small-z cell	PDI/WS ₂ supercell
a (Å)	3.164	12.657	12.657
b (Å)	3.164	25.314	25.314
c (Å)	30	15	30
a_B (Å)	21	5	X: 29, Y: 16
E_g (eV)	2.85	4.06	X: 2.78, Y: 2.72

Supplementary Table 2. Computed lattice parameters. Ab initio GW-BSE calculation-derived lattice parameters for WS₂, PDI, and PDI/WS₂. Crystallographic axes a , b , c ; exciton Bohr radii a_B ; quasiparticle direct gap E_g .

TMD	Temperature (°C)	Time/MOCVD cycle (hours)	Mo/W source flow (sccm)^(a)	S source flow (sccm)^(b)
MoS ₂	~500	15	0.6	0.3
WS ₂	~600	10	2.0	0.3
HBC	Temperature (°C)	Time/PVD cycle (hours)	Number of PVD cycles	Pressure (torr)^(c)
PDI/MoS ₂	275	6	2	6 × 10 ⁻⁴
PTCDA/MoS ₂	250	4	2	2 × 10 ⁻²
PDI/WS ₂	275	6	1	6 × 10 ⁻⁴
PTCDA/WS ₂	250	4	1	2 × 10 ⁻²
MePDI/WS ₂	280	6	2	6 × 10 ⁻⁴
C5-PDI/MoS ₂	280	4	4	2 × 10 ⁻²
C8-PDI/MoS ₂	280	4	4	2 × 10 ⁻²
PhPDI/WS ₂	280	4	4	6 × 10 ⁻⁴
PDI/hBN ^(d)	280	6	5	6 × 10 ⁻⁴
PDI/graphene ^(d)	275	6	2	6 × 10 ⁻⁴
PDI/hBN/graphene ^(d)	280	6	5	6 × 10 ⁻⁴
THPP/MoS ₂ ^(e)	265	8	1	6 × 10 ⁻³

(a) Metal sources: Mo(CO)₆ for Mo; W(CO)₆ for W

(b) Chalcogen (S) source: (C₂H₅)₂S

(c) Three quartz tube furnaces were employed to grow the molecular crystals having base pressures of 6 × 10⁻³ torr, 6 × 10⁻⁴ torr, and 2 × 10⁻² torr with tube diameters 1", 2", and 3", respectively.

(d) Graphene and hBN were mechanically exfoliated and transferred on SiO₂/Si substrate prior to growth.

(e) THPP: 5, 10, 15, 20-Tetrakis(4-hydroxyphenyl)porphine

Supplementary Table 3. Reaction conditions for different HBCs. Different vapor-phase deposition (MOCVD and PVD) conditions used to synthesize TMDs and HBCs.

Supplementary References

1. Perdew, J. P., Burke, K. & Ernzerhof, M. Generalized Gradient Approximation Made Simple. *Phys. Rev. Lett.* **77**, 3865–3868 (1996).
2. Grimme, S., Antony, J., Ehrlich, S. & Krieg, H. A consistent and accurate ab initio parametrization of density functional dispersion correction (DFT-D) for the 94 elements H-Pu. *J. Chem. Phys.* **132**, 154194 (2010).
3. Giannozzi, P. *et al.* QUANTUM ESPRESSO: A modular and open-source software project for quantum simulations of materials. *J. Phys. Condens. Mat.* **21**, 465901 (2009).
4. Giannozzi, P. *et al.* Advanced capabilities for materials modelling with Quantum ESPRESSO. *J. Phys. Condens. Mat.* **29**, 395502 (2017).
5. Hamann, D. R. Optimized norm-conserving Vanderbilt pseudopotentials. *Phys. Rev. B Condens. Matter Mater. Phys.* **88**, 085117 (2013).
6. Schlipf, M. & Gygi, F. Optimization algorithm for the generation of ONCV pseudopotentials. *Comput. Phys. Commun.* **196**, 36–44 (2015).
7. Adeniran, O. & Liu, Z. F. Quasiparticle electronic structure of phthalocyanine:TMD interfaces from first-principles GW. *J. Chem. Phys.* **155**, 214702 (2021).
8. Hedin, L. New Method for Calculating the One-Particle Green's Function with Application to the Electron-Gas Problem*. *Phys. Rev.* **139**, A 796–A 823 (1965).
9. Strinati, G., Mattausch, H. J. & Hanke, W. Dynamical Aspects of Correlation Corrections in a Covalent Crystal. *Phys. Rev. B* **25**, 2867–2888 (1982).
10. Hybertsen, M. S. & Louie, S. G. Electron Correlation in semiconductors and Insulators: Band Gaps and Quasiparticle Energies. *Phys. Rev. B* **34**, 5390–5413 (1986).
11. Deslippe, J. *et al.* BerkeleyGW: A massively parallel computer package for the calculation of the quasiparticle and optical properties of materials and nanostructures. *Comput. Phys. Commun.* **183**, 1269–1289 (2012).
12. Deslippe, J., Samsonidze, G., Jain, M., Cohen, M. L. & Louie, S. G. Coulomb-hole summations and energies for GW calculations with limited number of empty orbitals: A modified static remainder approach. *Phys. Rev. B* **87**, 165124 (2013).
13. Ismail-Beigi, S. Truncation of periodic image interactions for confined systems. *Phys. Rev. B Condens. Matter Mater. Phys.* **73**, 233103 (2006).

14. Ramasubramaniam, A. Large excitonic effects in monolayers of molybdenum and tungsten dichalcogenides. *Phys. Rev. B Condens. Matter Mater. Phys.* **86**, 115406 (2012).
15. Liu, Z. F., Da Jornada, F. H., Louie, S. G. & Neaton, J. B. Accelerating GW-Based Energy Level Alignment Calculations for Molecule-Metal Interfaces Using a Substrate Screening Approach. *J. Chem. Theory Comput.* **15**, 4218–4227 (2019).
16. Ulman, K. & Quek, S. Y. Organic-2D Material Heterostructures: A Promising Platform for Exciton Condensation and Multiplication. *Nano Lett.* **21**, 8888–8894 (2021).
17. Ud Din, N. & Liu, Z. F. Anisotropy of the Optical Properties of Pentacene:Black Phosphorus Interfaces. *J. Phys. Chem. C* **126**, 20694–20701 (2022).
18. Sharifzadeh, S., Darancet, P., Kronik, L. & Neaton, J. B. Low-energy charge-transfer excitons in organic solids from first-principles: The case of pentacene. *J. Phys. Chem. Lett.* **4**, 2197–2201 (2013).
19. Sharifzadeh, S. *et al.* Relating the Physical Structure and Optoelectronic Function of Crystalline TIPS-Pentacene. *Adv. Funct. Mater* **25**, 2038–2046 (2015).
20. Gutiérrez-Lezama, I., Ubrig, N., Ponomarev, E. & Morpurgo, A. F. Ionic gate spectroscopy of 2D semiconductors. *Nat. Rev. Phys.* **3**, 508–519 (2021).
21. Kang, K. *et al.* Layer-by-layer assembly of two-dimensional materials into wafer-scale heterostructures. *Nature* **550**, 229–233 (2017).
22. Zannotti, M. *et al.* Aggregation and metal-complexation behaviour of THPP porphyrin in ethanol/water solutions as a function of pH. *Spectrochim. Acta A Mol. Biomol. Spectrosc.* **193**, 235–248 (2018).
23. Chowdhury, T *et al.* Substrate-directed synthesis of MoS₂ nanocrystals with tunable dimensionality and optical properties. *Nat. Nanotechnol.* **15**, 29–34 (2020).
24. Kang, K. *et al.* High-mobility three-atom-thick semiconducting films with wafer-scale homogeneity. *Nature* **520**, 656–660 (2015).